

Human model of primary carnitine deficiency cardiomyopathy reveals ferroptosis as a novel disease mechanism

Malte Loos

University Medical Center Hamburg-Eppendorf

Birgit Klampe

University Medical Center Hamburg-Eppendorf

Thomas Schulze

University Medical Center Hamburg-Eppendorf

Xiaohe Yin

King's College London <https://orcid.org/0000-0002-5172-0935>

Konstantinos Theofilatos

KCL <https://orcid.org/0000-0001-6799-0553>

Bärbel Ulmer

University Medical Center Hamburg-Eppendorf

Carl Schulz

University Medical Center Hamburg-Eppendorf

Charlotta Behrens

University Medical Center Hamburg-Eppendorf

Tessa Van Bergen

Max Delbrück Center for Molecular Medicine in the Helmholtz Association

Eleonora Adami

Max-Delbruck-Center for Molecular Medicine (MDC)

Henrike Maatz

Centre for Molecular Medicine- MDC

Michaela Schweizer

Center for Molecular Neurobiology Hamburg (ZMNH), University Medical Center Hamburg-Eppendorf, Hamburg

Susanne Brodesser

CECAD Research Center <https://orcid.org/0000-0001-5631-0663>

Boris Skryabin

Muenster University Hospital

Timofey Rozhdestvensky

University of Muenster <https://orcid.org/0000-0002-3384-925X>

Sara Bodbin

University of Nottingham

Torsten Christ

University Medical Center Hamburg-Eppendorf <https://orcid.org/0000-0002-8935-5304>

Chris Denning

University of Nottingham

Norbert Huebner

Max Delbrück Center for Molecular Medicine in the Helmholtz Association (MDC)

<https://orcid.org/0000-0002-1218-6223>

Manuel Mayr

King's College London British Heart Foundation Centre, School of Cardiovascular Medicine and Sciences, London <https://orcid.org/0000-0002-0597-829X>

Thomas Eschenhagen

University of Hamburg <https://orcid.org/0000-0003-1750-1170>

Arne Hansen (✉ ar.hansen@uke.de)

University Medical Center Hamburg-Eppendorf

Article**Keywords:**

Posted Date: August 11th, 2022

DOI: <https://doi.org/10.21203/rs.3.rs-1880728/v1>

License:  This work is licensed under a Creative Commons Attribution 4.0 International License.

[Read Full License](#)

1 **Titel**

2 **Human model of primary carnitine deficiency cardiomyopathy reveals ferroptosis as a**
3 **novel disease mechanism**

4 **Authors**

5 Malte Loos^{1,2}, Birgit Klampe¹, Thomas Schulze¹, Xiaoke Yin³, Konstantinos Theofilatos³, Bärbel Maria
6 Ulmer^{1,2}, Carl Schulz^{1,2}, Charlotta Behrens^{1,2}, Tessa Diana van Bergen⁴, Eleonora Adami⁴, Henrike
7 Maatz⁴, Michaela Schweizer⁵, Susanne Brodesser⁶, Boris V. Skryabin⁷, Timofey S. Rozhdestvensky⁷,
8 Sara Bodbin⁸, Torsten Christ^{1,2}, Chris Denning⁸, Norbert Hübner^{4,9,10}, Manuel Mayr³, Thomas
9 Eschenhagen^{1,2}, Arne Hansen^{1,2}

10 **Affiliations**

11 ¹University Medical Center Hamburg-Eppendorf, Department of Experimental Pharmacology and
12 Toxicology, 20246 Hamburg, Germany

13 ²German Center for Heart Research (DZHK), Partner site Hamburg/Lübeck/Kiel, Germany

14 ³King's British Heart Foundation Centre of Research Excellence, King's College London, United Kingdom

15 ⁴Cardiovascular and Metabolic Sciences, Max Delbrück Center for Molecular Medicine in the
16 Helmholtz Association (MDC), 13125 Berlin, Germany

17 ⁵Electron Microscopy Unit, Center for Molecular Neurobiology Hamburg, University Medical Center
18 Hamburg-Eppendorf, 20251 Hamburg, Germany

19 ⁶Cluster of Excellence Cellular Stress Responses in Aging-associated Diseases (CECAD), Faculty of
20 Medicine and University Hospital of Cologne, 50931 Cologne, Germany

21 ⁷Transgenic animal and genetic engineering Models (TRAM), Faculty of Medicine of the Westfalian
22 Wilhelms-University, 48149 Muenster, Germany

23 ⁸Division of Cancer & Stem Cells, Biodiscovery Institute, University of Nottingham, NG7 2RD, United
24 Kingdom.

25 ⁹DZHK (German Centre for Cardiovascular Research), Partner Site Berlin, 13347 Berlin, Germany

26 ¹⁰Charité -Universitätsmedizin, 10117 Berlin, Germany

27 **Contact**

28 Malte Loos (m.loos@uke.de)

29 Arne Hansen (ar.hansen@uke.de)

30 Abstract

31 Primary carnitine deficiency (PCD) is an autosomal recessive monogenic disorder caused by
32 mutations in *SLC22A5*. This gene encodes for OCTN2 which transports the essential metabolite
33 carnitine into the cell. PCD patients suffer from muscular weakness and dilated
34 cardiomyopathy. Detailed molecular disease mechanisms remain unclear. Two OCTN2-
35 defective human induced pluripotent stem cell lines were generated from a healthy control
36 line, carrying a full OCTN2-knockout and a homozygous OCTN2 (N32S) loss of function
37 mutation. OCTN2-defective genotypes showed lower cardiac differentiation efficiency, lower
38 force development, and resting length in engineered heart tissue format compared to isogenic
39 control. Force was sensitive to fatty acid-based media and associated with lipid accumulation,
40 mitochondrial alteration, higher glucose uptake, and metabolic remodelling, replicating
41 findings in animal models. Importantly, genome wide analysis and pharmacological inhibitor
42 experiments identified ferroptosis, an iron- and lipid-dependent cell death pathway linked to
43 fibroblast activation as a novel PCD cardiomyopathy disease mechanism.

44 Introduction

45 Primary carnitine deficiency (PCD) is an autosomal recessive disorder resulting in insufficient
46 cellular carnitine (β -hydroxy- γ -trimethylammonium butyrate) uptake and low cytoplasmic
47 concentrations ¹. PCD is caused by pathogenic variants in the *SLC22A5* gene, leading to loss of
48 function of the encoded organic cation transporter novel family member 2 (OCTN2). OCTN2 is
49 strongly expressed in the myocardium, skeletal muscle, fibroblasts, renal tubules, placental
50 tissue and intestine ². OCTN2 transports carnitine in a sodium-dependent manner and
51 maintains intracellular carnitine concentrations 20-50-fold higher than in the extracellular
52 space ^{3,4}. In the cytoplasm, carnitine palmitoyltransferase 1 (CPT1) catalyzes the formation of
53 acylcarnitine from carnitine and long chain acyl-CoA . The carnitine-acylcarnitine translocase
54 (CACT) transports acylcarnitine across the mitochondrial membrane into the mitochondria,
55 where carnitine palmitoyltransferase 2 (CPT2) reconverts acylcarnitine to acyl-CoA that
56 subsequently enters beta-oxidation. Low cytoplasmic carnitine concentration impairs fatty
57 acid beta-oxidation leading to insufficient ATP generation under high workload conditions and
58 cytoplasmic lipid accumulation. This results in glucose-dependency as energy metabolism,
59 inhibited gluconeogenesis (due to inhibition of pyruvate carboxylase) and diminished
60 ketogenesis (due to a lack of acetyl-CoA derived from beta-oxidation) ¹. The strong reliance of
61 cardiomyocytes on fatty acids as energy substrate makes the heart particularly susceptible to
62 PCD pathomechanisms. Apart from the mitochondrial fatty acid transfer, carnitine
63 conjugation has a crucial role to reduce the number of coenzyme A (CoA) molecules attached
64 to acyl residues. Excessive accumulation of cytoplasmic acyl-CoA results in the formation of
65 ceramides, TAG and cholesteryl-ester that were reported to induce inflammation and
66 apoptosis in different organs ⁵.

67 Typical clinical PCD symptoms are hypoglycemia and hypoketonemia under fasting conditions,
68 liver dysfunction, muscular weakness and dilated cardiomyopathy (DCM) ^{6,7}. Symptomatic
69 patients are typically diagnosed in the first five years of life and receive a lifetime treatment
70 with high dose of carnitine (100–200 mg/kg/day)⁶. Despite inhibited cellular uptake, PCD
71 patients have low plasma carnitine concentrations (0-5 μ mol/l, physiological: 25-50 μ mol/l ⁸)
72 because OCTN2-mediated carnitine reabsorption in renal proximal tubules system is
73 impaired ⁹. Relevant side effects of carnitine supplementation include nausea, vomiting,
74 abdominal cramps, diarrhea, a fishy body odor, and accumulation of atherogenic
75 trimethylamine N-oxide (TMAO) ¹⁰⁻¹². Moreover, numerous untreated PCD patients reach

76 adulthood and remain asymptomatic but still have an increased risk for sudden cardiac death
77 ^{13,14}. Detailed mechanisms of the PCD DCM remain poorly understood.

78 PCD is a rare disease. Prevalence range from 1:20,000–1:70,000 (United States) ⁷, 1:120,000
79 (Australia) ¹⁵ to 1:8000 - 1:17,000 (China) ^{16,17}. The Faroe Island, an isolated archipelago in the
80 Northern Atlantic, has by far the highest prevalence with 1:300 ⁹. The overall approximate
81 allelic frequency of *SLC22A5* pathogenic variants in the population is 0.5-1%. *SLC22A5* was
82 recently reported to be frequently associated with autosomal recessive mitochondrial
83 disorders in gnomAD ¹⁸. Pathogenic variants were found in all *SLC22A5* exonic coding regions
84 but are often located in the first exon of the *SLC22A5* gene ¹⁹. The *SLC22A5* c.95A>G (N32S)
85 mutation is the characteristic PCD mutation on Faroe Island ⁹.

86 Juvenile visceral steatosis (JVS) mice are an animal model of carnitine deficiency ²⁰. This strain
87 was discovered by coincidence to have an OCTN2 p.L352R missense mutation ²¹. JVS mice
88 demonstrate high renal carnitine excretion and tissue lipid accumulation in the first week and
89 hyperammonaemia, hypoglycemia, hepatic microvesicular steatosis, and growth retardation
90 three weeks after birth ²². JVS mice develop cardiac hypertrophy 10 days after birth associated
91 with cardiac steatosis, accumulation of diacylglycerols (DAG) and triglycerides (TAG), but no
92 ceramide ²³, lower myocardial ATP content ²⁴, and high expression of the pyruvate
93 dehydrogenase (PDH) inhibitor PDH kinase 4 (*PDK4*) ²⁵. A pharmacological carnitine deficiency
94 animal model was established by administering the competitive OCTN2- and BBOX1 (γ
95 butyrobetaine hydroxylase) inhibitor *N*-trimethyl-hydrazine-3-propionate (THP) to wildtype
96 rats for three weeks. The rats revealed increased renal carnitine excretion and hepatic
97 steatosis but no cardiac or skeletal phenotype ²⁶. Compensatory upregulation of proteins
98 involved in the carnitine shuttle system, such as CPT1 has been previously described ^{27,28}. No
99 human induced pluripotent stem cell (hiPSC) model of PCD has been published so far.

100 The aim of this study was the development of a predictive hiPSC model of PCD DCM. Two
101 hiPSC lines derived from an established control hiPSC line (OCTN2 (+/+)) were generated by
102 CRISPR/Cas9 technology. The lines carried either a full OCTN2-knockout (OCTN2 (-/-)) or the
103 homozygous missense founder mutation (OCTN2 (N32S), *SLC22A5* c.95A>G) characteristic for
104 PCD patients from the Faroe Islands ^{9,29}. Cardiomyocytes were differentiated, and the PCD
105 disease phenotype was analyzed in genome-wide, molecular, functional (contractility), and
106 morphological assays. These experiments show that this hiPSC PCD model replicates a wide

107 range of PCD DCM characteristics found in patients and animal models and moreover reveals
108 ferroptosis linked to fibroblast activation as a novel disease mechanism.

109 Results

110 CRISPR/Cas9

111 An established control hiPSC line (OCTN2 (+/+)) was used for the CRISPR/Cas9 engineering
112 approach and served as the isogenic control. The CRISPR/Cas9 strategy is presented in
113 Supplementary Figure 1A, B. A representative Sanger sequencing trace of successfully edited
114 clones is depicted in Supplementary Figure 2A and shows the OCTN2 wildtype sequence
115 (upper lane) and the heterozygous silent point mutation (c.277C>T) in the isogenic control
116 hiPSC line. The middle lane shows the homozygous introduction of the OCTN2 (N32S) c.95A>G
117 founder point mutation in exon 1 of the *SLC22A5* gene. Due to the large deletion, Sanger
118 sequencing trace of OCTN2 (-/-) in the lower lane could not be aligned. PCR products derived
119 from internal and flanking primers of both CRISPR cutting sites in the OCTN2 (+/+) hiPSC line
120 are shown in Supplementary Figure 2B-E. The successful knockout was confirmed by
121 quantitative reverse transcription PCR (qPCR) of the *SLC22A5* transcript (Supplementary
122 Figure 2C). Southern blots validated the integrity of the edited locus. Supplementary Figure
123 3A displays the predicted cutting sites for the two restriction endonucleases HindIII and EcoRI
124 of the *SLC22A5* gene. Predicted fragment size and Southern blot results are shown in
125 Supplementary Figure 3B and C. Nanostring nCounter human karyotype assay revealed
126 normal karyotype for all lines (Supplementary Figure 4).

127 Functional analysis

128 Cardiomyocytes were successfully differentiated from all 3 hiPSC lines. Supplementary Figure
129 5A shows no difference in the percentage of cardiac troponin T (cTnT) positive cells for the
130 cardiac differentiation experiments between the three lines (OCTN2 (+/+) 87.5±2.5%, n= 10
131 differentiations; OCTN2 (N32S): 84.1±5.0%, n= 10 differentiations; OCTN2 (-/-): 86.2±8.2%, n=
132 9 differentiations). Cardiac differentiation efficiency (output-hiPSC-CM / input-hiPSC cells)
133 revealed significantly lower differentiation efficiency for OCTN2 (N32S) (23.5±10.5%) and
134 OCTN2 (-/-) (19.4±2.8%) compared to OCTN2 (+/+) (79.0±10.0%) (Supplementary Figure 5B).

135 Engineered Heart Tissue (EHT) samples were subjected to video-optical force analysis under
136 spontaneous beating conditions starting on day 7 (Supplementary Figure 5C-H). Contractile
137 parameters changed in EHTs from all three cell lines and reached a plateau after day 21.
138 OCTN2 (-/-) showed a lower force, higher contraction time and shorter resting length for the

139 entire culture time. Beating frequency was higher for OCTN2 (N32S) and OCTN2 (-/-) during
140 the initial phase of development, but not thereafter. Relaxation time was longer only for
141 OCTN2 (-/-) for the last 2 weeks of development. No difference could be detected for the RR
142 scatter as a surrogate for arrhythmic beating. Contractile values of day 21 were compared
143 (Figure 1A - F) and showed lower force and a shorter resting length for OCTN2 (-/-) compared
144 to OCTN2 (+/+) (OCTN2 (+/+): 0.194 ± 0.004 mN, n= 153 EHTs; OCTN2 (N32S): 0.16 ± 0.01 mN,
145 n= 108 EHTs; OCTN2 (-/-): 0.11 ± 0.01 mN, n= 91 EHTs). Both OCTN2-defective genotypes
146 exhibited a higher contraction time, and OCTN2 (-/-) a higher relaxation time. Figure 2A, B
147 depict representative average contraction peaks and video-optical EHT images. A
148 representative video of EHTs from all three genotypes can be found in the supplement
149 (Supplementary Video 1-3). The contractile phenotype was associated with a shorter APD₉₀ of
150 211.0 ± 13.6 (SEM, n=7) in OCTN2 (N32S) versus 288.2 ± 15.5 (SEM, n=9) in OCTN2 (+/+) as
151 measured by sharp microelectrode protocol (Figure 2C, D). Importantly, force and resting
152 length of both OCTN2-defective genotypes showed a positive correlation with the
153 cardiomyocyte purity of the input cell population (Figure 3A, B), implying an important role of
154 non-cardiomyocytes. To study the ability to metabolize long-chain fatty acids (LCFA), EHTs
155 were switched to a medium containing only LCFA plus carnitine [50 μ M]. Force remained
156 stable in OCTN2 (+/+) EHTs but declined in OCTN2-defective EHTs (Figure 3C), indicating a
157 reduced ability to metabolize LCFA.

158 Delta glucose and lactate values were higher for OCTN2 (N32S), but not OCTN2 (-/-) compared
159 to OCTN2 (+/+). The delta lactate/delta glucose ratio as a surrogate for anaerobic glucose
160 metabolism showed no difference (Supplementary Figure 6A-C). Higher glucose consumption
161 for OCTN2 (N32S) and OCTN2 (-/-) became evident when normalised to workload (force x
162 beating frequency) (OCTN2 (+/+): 0.23 ± 0.01 mM/bpm \times mN; OCTN2 (N32S): 0.3 ± 0.1 mM;
163 OCTN2 (-/-): 0.4 ± 0.1 mM) (Figure 3D).

164 Proteomics, Seahorse

165 3,425 proteins were detected by tandem mass tag (TMT)-based proteomic analysis, of which
166 1,772 proteins differed significantly between OCTN2 (+/+) and OCTN2 (N32S) and 2050
167 differed significantly between OCTN2 (+/+) and OCTN2 (-/-), respectively ($p < 0.05$). A detailed
168 summary of detected proteins is shown in Supplementary Table 1. Principal component
169 analysis revealed separate clustering of OCTN2 (+/+) from OCTN2 (N32S), and OCTN2 (-/-)

170 (Figure 4A). Volcano plot depiction highlights a higher abundance of fibrosis-related- and
171 extracellular matrix proteins like caldesmon1 (CALD1), collagen type I alpha 1 chain (COL1A1),
172 transgelin 2 (TAGLN2), fibronectin 1 (FN1) and vitronectin (VTN) in OCTN2 (N32S) EHTs (Figure
173 4B). Moreover, ceramide transfer protein (CERT) was among the 10 most abundant proteins
174 in OCTN2 (N32S). In contrast, the fatty acid transporters cluster of differentiation 36 (CD36),
175 fatty acid-binding protein 5 (FABP5) and cardiomyogenesis transcriptional regulator GATA
176 binding protein 4 (GATA4) were among the top 10 lower abundant proteins in OCTN2 (N32S).
177 Detailed grouping of proteins related to their participation in pathways, such as cardiac
178 physiology, lipid metabolism, glycolysis, carnitine shuttle, electron transport chain, TCA cycle,
179 and beta-oxidation revealed a concordant expression pattern for both, OCTN2 (N32S) and
180 OCTN2 (-/-) versus OCTN2 (+/+) (Figure 4C). KEGG pathway overrepresentation analysis
181 revealed enrichment of N-glycan- and O-glycan biosynthesis, ferroptosis, and cholesterol
182 metabolism in OCTN2 (N32S) high abundant proteins. Conversely, enrichment analysis of
183 lower abundant proteins in OCTN2 (N32S) revealed the KEGG pathways pyruvate- and
184 propanoate metabolism, glycolysis, pentose phosphate pathway glyoxylate and dicarboxylate
185 metabolism, and different pathways associated with amino acid metabolism (Figure 4D). A
186 detailed summary of specific proteins in the enriched pathways is depicted in Supplementary
187 Table 2 and 3. Quantification of mitochondrial DNA revealed a lower level in OCTN2 (N32S),
188 indicating lower abundance of mitochondria. Both OCTN2-defective lines showed lower
189 oxygen consumption rate und baseline, oligomycin, FCCP and rotenone conditions in Seahorse
190 experiments (Supplementary Figure 7A, B).

191 Carnitine supplementation: Acylcarnitine and ceramide content, force, lipid mass
192 spectrometry, TEM

193 EHT media was supplemented with carnitine (2 mM) for the entire culture time. This was
194 accompanied by a reduction of glucose consumption and lactate production for all genotypes
195 (Supplementary Figure 8A-C). Notably, glucose consumption normalized to cardiac workload
196 was reduced only for the two OCTN2-defective cell lines (Figure 5A). This was associated with
197 a small increase in force for all cell lines (Figure 5B, C) and a substantial increase in relaxation
198 time (Supplementary Figure 8D-G). Notably, transcript levels of PDK4, the inhibitor of PDH and
199 important metabolic regulator, were higher in OCTN2 (N32S) versus OCTN2 (+/+) and
200 attenuated to isogenic control level by carnitine supplementation (Supplementary Figure 8H).

201 Liquid chromatography–mass spectrometry (LC-MS) revealed 5-fold lower content for C16:1-
202 , C18:0-, C18:1- and C18:2 acylcarnitines in OCTN2 (N32S) compared to OCTN2 (+/+). Carnitine
203 supplementation resulted in a higher content of C16:0-, C16:1-, C18:1- and C18:2
204 acylcarnitines for OCTN2 (+/+) and C18:1-, C18:2 acylcarnitines for OCTN2 (N32S). Ceramides
205 are one metabolite of accumulated cytoplasmic acyl-CoA. Quantification of ceramide content
206 (Cer16:0, Cer18:0, Cer22:0, Cer24:0, Cer24:1) revealed no difference between the genotypes
207 and no effect of carnitine supplementation (Figure 5D, E).

208 Transmission electron microscopy (TEM, Figure 6A-F)) showed elongated myofilaments and
209 structured mitochondria in OCTN2 (+/+) EHTs. OCTN2 (N32S) displayed a lower abundance of
210 mitochondria and structural mitochondrial defects, and a high frequency of large lipid droplets
211 in close association with mitochondria and sarcomeres. OCTN2 (-/-) also exhibited
212 mitochondria with degraded structure and increased membrane density but no pronounced
213 aggregation of lipid droplets. Carnitine supplementation appeared to increase mitochondria
214 frequency for all genotypes and to reduce the frequency of lipid droplets for the OCTN2-
215 defective genotypes.

216 Single nuclear RNA sequencing

217 A pool of 4 EHTs per genotype was subjected to single nuclear RNA sequencing (snRNA seq).
218 OCTN2 (+/+), (N32S) and (-/-) samples were sequenced with an average sequencing depth of
219 39,324, 28,771 and 26,374 read pairs per nucleus. Following quality control filtering, snRNA
220 seq data of all three genotypes were pooled to a total number of 11,225 nuclei ((OCTN2 (+/+) = 3,135,
221 OCTN2 (N32S) = 3,761, OCTN2 (-/-) = 4,329 cells). Uniform manifold approximation
222 and projection (UMAP) and leiden clustering revealed 5 main cell clusters. Marker genes for
223 these clusters delineated: cardiomyocytes, proliferating cardiomyocytes, fibroblasts,
224 endothelial and myeloid cells (Figure 7A). In OCTN2 (+/+), cardiomyocytes represented 94% of
225 all cells with 14% of these cells showing markers of proliferation (Figure 7B, C). Sub-clustering
226 of cardiomyocytes revealed 10 subclusters (Supplementary Figure 9). Subcluster CM4 was
227 dominant in OCTN2 (+/+), while subclusters 1 and 2 were more prominent in OCTN2-defective
228 lines. Interestingly, KEGG analysis revealed enrichment of the GPR40 pathway in CM4,
229 describing free fatty acid receptor 1 signalling (Supplementary Figure 9C). A lower
230 representation of CM4 in the OCTN2-defective lines is compatible with the lower abundance
231 of fatty acid transporters in the proteomics analysis. In OCTN2 defective lines, cardiomyocytes

232 represented a smaller fraction of all cells (OCTN2 (N32S): 85%, OCTN2 (-/-): 67%). Reversely,
233 these lines showed a higher fraction of fibroblasts (OCTN2 (+/+): 4%, OCTN2 (N32S): 10%,
234 OCTN2 (-/-): 23%), (Figure 7B, C). Sub-clustering of fibroblasts identified 4 states. Fibroblasts
235 states with markers of TGF-beta signaling, proliferation and secretion (FB1, FB3, FB4), were
236 more prominent in OCTN2-defective lines (Figure 7D, E, F, Supplementary Figure 10A).
237 Genotype-specific analysis of significant KEGG pathway enrichment in all fibroblast subcluster
238 revealed relaxin-, ECM- and focal adhesion-related pathways (Supplementary Figure 10B).

239 Endothelial and myeloid cells were almost absent in OCTN2 (+/+) and represented 5% and 1%
240 in OCTN2 (N32S) and 8% and 1% in OCTN2 (-/-) respectively (Figure 7B). Endothelial cells
241 expressed PDE3A, CASC15 and the typical marker gene MECOM, myeloid cells expressed
242 PTPRC (CD45), CD163 and AOA1 (Figure 7C). Comparative analysis of significant KEGG
243 pathway enrichment was not possible because significant pathways could only be detected
244 for OCTN2 (-/-) endothelial cells (Supplementary Figure 10B).

245 Ferroptosis, fibroblast activation

246 Proteomics analysis revealed enrichment of proteins related to the KEGG pathway ferroptosis,
247 an iron-dependent lipid peroxidation-mediated cell death mechanism. Extraction of an
248 extended list of pro- and anti-ferroptotic proteins³⁰ from the proteomics data set identified a
249 strikingly uniform regulation with a higher abundance of pro- and a lower abundance of anti-
250 ferroptotic proteins in the OCTN2-defective genotypes (Figure 8A). Noteworthy among these
251 were also the key regulators ACSL4³¹ and LPCAT3. These two proteins synergistically drive the
252 accumulation of iron-dependent lethal lipid peroxides (LPO)³². On the other hand, pro- and anti-
253 ferroptosis transcripts did not show a differential expression in snRNA seq, suggesting a post-
254 transcriptional regulation (Figure 8B). Evidence for ferroptosis and fibroblast activation in this
255 study and previous reports demonstrating a mechanistic link between these two pathways
256^{33,34} were the reason to analyse the effect of the potent ferroptosis inhibitor liproxstatin on
257 fibrosis markers. OCTN2 (N32S) EHTs revealed higher transcript levels of *ACTA2*, *COL1A1*,
258 *POSTN*, *TGFB*, *FN*, and *CCN2* than OCTN2 (+/+). Liproxstatin induced a significant attenuation
259 of fibrosis transcript levels in OCTN2 (N32S), which was associated with a moderate increase
260 in force development (Figure 8C-D).

261 Discussion

262 This study aimed to establish a human PCD DCM *in vitro* model. The main results of this work
263 are 1: successful genetic engineering of two experimental hiPSC lines, a homozygous
264 OCTN2 (N32S) and an OCTN2 (-/-) knockout hiPSC line; 2: Replication of the PCD DCM
265 phenotype in the hiPSC PCD model by low acylcarnitine tissue content and low force
266 development, complex metabolic remodeling, and ultrastructural alteration; 3: Validation of
267 the of OCTN2 (N32S) loss-of-function disease phenotype by high-level concordance with the
268 OCTN2 (-/-) knockout hiPSC line across various assays; 4: Discovery of ferroptosis activation
269 linked to fibroblast activation as novel PCD DCM mechanism.

270 The role of *SLC22A5* in hiPSC biology is not yet understood. RNA sequencing data from Liu et
271 al.³⁵ demonstrated a continuous expression of *SLC22A5* during all stages of hiPSC
272 cardiomyocyte differentiation, suggesting the relevance of carnitine metabolism throughout
273 this process. OCTN2-defective hiPSC lines might therefore be compromised during cardiac
274 differentiation. Compatible with this, the OCTN2 (+/+) control hiPSC line outperformed both
275 OCTN2-defective hiPSC lines with respect to differentiation efficiency (cardiomyocyte output
276 in relation to the input of hiPSC). The approach to engineer the human-relevant OCTN2 (N32S)
277 loss of function point mutation in parallel with a complete OCTN2 knockout turned out to be
278 very insightful since the concordant changes of several parameters (e.g. contractile
279 parameters, protein expression of metabolic markers, clustering of (non)-cardiomyocyte
280 subpopulations) in both defective lines validated the implication of OCTN2.

281 Typical features of PCD DCM in both patients and established animal models are markedly
282 reduced tissue contents of different carnitine derivates, functional impairment of glucose and
283 lipid metabolism, myocardial steatosis, severe hyperglycemia^{22,24} and short QT syndrome^{36,37}.
284 Several key aspects could be replicated in this hiPSC-CM model: OCTN2-defective EHTs
285 revealed lower force and higher sensitivity of force to fatty acid-based media, reduced
286 acylcarnitine tissue content intracellular lipid droplet accumulation, and shorter action
287 potential duration. Genome-wide analysis revealed complex metabolic remodeling and
288 mitochondrial dysfunction. These alterations are compatible with (acyl)-carnitine deprivation
289 and have previously been described in PCD-animal models^{24,37}. Upregulation of carnitine
290 shuttle proteins likely represents a compensatory effect in response to carnitine deprivation,
291 similar to findings in secondary carnitine deficiency animal models^{38,39}. Moreover, this model

292 showed a lower abundance of glycolytic proteins but higher glucose uptake. This is compatible
293 with the poor correlation between glycolytic enzyme abundance and glycolysis in previous
294 studies ⁴¹.

295 One consequence of low cytoplasmic carnitine concentration is a decrease of acylcarnitine
296 formation and subsequent beta-oxidation ⁸. Indeed, mass spectrometry analysis revealed
297 lower tissue content of several long-chain acylcarnitines in OCTN2 (N32S) EHTs. In addition,
298 declining force in LCFA media suggested a defect in LCFA metabolism. Surprisingly, mass
299 spectrometry did not reveal a difference in ceramide content between the genotypes.
300 However, ceramides do not represent the final product but a metabolic intermediate that can
301 be processed to sphingolipid derivatives such as glucosylceramides and sphingomyelin ⁴². For
302 this conversion, ceramides are transported from the endoplasmic reticulum (ER) into the
303 trans-Golgi apparatus by the ceramide transporter CERT ⁴³. Remarkably, CERT was among the
304 10 most significantly higher abundant proteins in OCTN2 (N32S) EHTs, suggesting that it
305 belongs to the compensatory mechanisms and prevents the accumulation of toxic ceramides.

306 Carnitine supplementation (2 mM) had a strong effect on metabolic aspects of the PCD disease
307 phenotype like acylcarnitine tissue content, glucose consumption per cardiac work, PDK4
308 transcript level and lipid droplet accumulation. Nevertheless, the force restoration was minor
309 and the carnitine-induced increase in force was in the same range for all three genotypes,
310 suggesting a non-specific effect potentially related to induction of sodium current and
311 subsequent inhibition of Na⁺/K⁺-ATPase as previously described ^{44,45}. The discrepancy
312 between strong metabolic and small force effects of carnitine supplementation suggests
313 additional mechanisms to be relevant. The shorter EHT resting length, the positive correlation
314 between cardiomyocyte percentage of the input cell population with force and resting length
315 and the enrichment of extracellular matrix KEGG pathway the OCTN2-defective genotypes
316 suggest fibrosis to be relevant. In support of this, snRNA seq revealed a more prominent
317 fibroblast cluster in the OCTN2 –defective genotypes, which expressed markers indicative of
318 activated and secretory state. Of note, markers of activated fibroblasts in this study (*POSTN*,
319 *FN1*, *FAP*, *NOX4*) overlap substantially with the fibroblast signatures in two failing heart snRNA
320 seq DCM studies ^{46,47}. Interestingly, the central role of fibroblasts in this hiPSC-CM PCD model
321 is paralleled by clinical findings of strong myocardial fibrosis in PCD patients ^{6,48,49}.

322 Proteomic analysis provided evidence for ferroptosis, an iron-dependent cell death
323 mechanism related to lipid peroxidation, to be relevant in this model. Ferroptosis is well
324 compatible with PCD DCM, since it is driven by the accumulation of polyunsaturated fatty
325 acids (PUFAs) linked to coenzyme A (CoA) in cell membranes⁵⁰. PUFA accumulation is relevant
326 for PCD as cytosolic carnitine deficiency impairs PUFA metabolization to acylcarnitine. ACSL4
327 catalyzes the esterification of long-chain PUFA to acyl-CoA and represents a central pro-
328 ferroptotic regulator⁵¹. This marker showed a higher expression and protein abundance in
329 this model. The abundance of the central anti-ferroptotic enzyme GPX4 was not lower in
330 OCTN2-defective lines in contrast to other ferroptotic proteins. Notably, glutathione is an
331 important cofactor for GPX4 activity and proteins involved in glutathione metabolism such as
332 Glutamate-Cysteine Ligase (GCLC), Glutathione Synthetase (GSS) and glutathione-disulfide
333 reductase (GSR) were lower abundant in OCTN2-defective lines.

334 Importantly, ferroptosis was recently shown to be linked to fibrosis development and
335 cardiomyopathy^{33,34}. Mechanistically, profibrotic factors released from ferroptotic cells were
336 identified to drive fibroblast activation³³. A similar mechanistic link is likely relevant in this
337 model since the ferroptosis inhibitor liproxstatin induced a reduction of fibrosis transcript
338 levels and higher force. Overall, the discovery of ferroptosis activation reveals novel insight
339 into the development of PCD-associated metabolic cardiomyopathy and is paving the way to
340 the development of specific antifibrotic treatment strategies.

341

342 Experimental procedures

343 HiPSC cell culture conditions

344 An established hiPSC control cell line (hiPSCreg code UKEi001-A) derived from a healthy
345 individual served as the starting point for the genetic engineering approach and as the isogenic
346 control for the engineered hiPSC lines. This hiPSC line was generated by reprogramming
347 dermal fibroblast from a skin biopsy using the CytoTune (Life Technologies) 2.0 Sendai
348 Reprogramming Kit under feeder-free conditions. All basic stem cell culture work was
349 performed as recently described⁵². In brief, hiPSC culture was based on the expansion of a
350 master cell bank (MCB) at passage 25-35 on Geltrex-coated cell culture flasks in FTDA-medium
351 (Supplementary Table 4) under hypoxic conditions (5% O₂). Standard passaging was
352 performed twice a week (3-4 day passaging interval) with Accutase solution (Sigma-Aldrich).
353 Plating density was 4.5-7.0×10⁴ hiPSC/cm². Maximal expansion was for 40 passages with
354 regular screening for mycoplasma contamination by PCR amplification. SSEA3 surface marker
355 served as a pluripotency marker and was analyzed by flow cytometry. All procedures involving
356 the generation and analysis of hiPSC lines were approved by the local ethics committee in
357 Hamburg (Az PV4798, 28.10.2014).

358 CRISPR/Cas9-mediated gene editing

359 OCTN2 (N32S) missense mutation

360 The *SLC22A5* gene locus was Sanger sequenced in the hiPSC OCTN2 (+/+) control line.
361 CRISPR/Cas9 technology was used to engineer the c.95A>G (N32S) mutation into the *SLC22A5*
362 wild type. IDT Custom Alt-R CRISPR-Cas9 gRNA software and CRISPOR⁵³ were used to identify
363 potential gRNA binding sites at the gene locus. The OCTN2 NCBI Reference (NG_008982.2)
364 was provided as a target sequence. Targets for gRNA's were chosen based on the lowest cut-
365 to-mutation distance under consideration of a high on-target potential and low off-target risk.
366 A single-stranded oligodeoxynucleotide (ssODN) served as an exogenous donor template,
367 containing the OCTN2 c.95A>G, p.N32S mutation. Additionally, a silent mutation was
368 introduced in the PAM sequence to prevent CRISPR/Cas9 re-cutting after successful genomic
369 integration of the template by HDR. Edited clones were identified by PCR amplification and
370 subsequent Sanger sequencing. A schematic overview of the HDR strategy is depicted in
371 Supplementary Figure 1A. SsODN- and gRNA sequences are shown in Supplementary Table 5.

372 OCTN2 (-/-) knockout

373 A combinatorial CRISPR strategy was used to engineer a knockout of the *SLC22A5* gene in the
374 isogenic control hiPSC OCTN2 (+/+). Two gRNA's were designed to introduce a deletion of 17.3
375 kb spanning from the promotor region to exon 5 (NG_008982.2). For deletion validation
376 primer pairs were designed to amplify products inside the deletion region and the gRNA target
377 sites. Also, primers flanking the two cutting sites were designed. Edited clones were identified
378 by PCR amplification and subsequent Sanger sequencing. A schematic overview of the
379 knockout strategy is displayed in Supplementary Figure 1B. To distinguish between unedited,
380 heterozygous and homozygous edited clones, the PCR products were separated by agarose
381 gel electrophoresis (1% (w/v)), followed by Midori green staining. The target gRNA sequences
382 are shown in Supplementary Table 5.

383 Nucleofection

384 The Amaxa™ P3 Primary Cell 4D-Nucleofector X Kit L (Lonza) was used for delivery of the
385 CRISPR/Cas9 ribonucleoprotein (RNP) complex into hiPSCs. A working cell bank aliquot of the
386 control hiPSC (passage 25-30) was cultured for at least 2 passages on a 6-well plate to reach
387 60-70% confluency on the day of nucleofection. HiPSCs were incubated with the apoptosis
388 inhibitor Y-27632 (10 μM) two hours prior to nucleofection. The fluorescence-labeled
389 tracrRNA-ATTO 550 (IDT) was used to monitor the electroporation efficiency. The tracrRNA
390 oligos and the CRISPR-Cas9 crRNA (IDT) oligos were resuspended in RNase-free IDTE Buffer
391 (IDT) to a final stock concentration of 100 μM. For gRNA duplex formation, 5 μL of crRNA (100
392 μM) were annealed with 5 μL tracrRNA (100 μM), incubated for 5 min at 95 °C and cooled
393 down to room temperature. For formation of the RNP- complex, 5 μL of the gRNA duplex were
394 mixed with 5 μL Cas9 protein (61 μM, IDT) and incubated for 1.5 hours at room temperature
395 under light protection. For the knockout approach 5 μL of the second gRNA duplex were added
396 to the suspension in addition. To prepare the nucleofector solution, 82 μL P3 reagent and 18
397 μL supplement reagent (Lonza) were mixed per reaction according to the instruction of the
398 Amaxa™ P3 Primary Cell 4D-Nucleofector X Kit L (Lonza). HiPSCs were washed twice with PBS
399 buffer and dissociated into single cells with 1 mL accutase solution (Sigma) per well at 37 °C.
400 The dissociation was stopped by adding 1 mL FTDA medium per 6-well. The hiPSCs were
401 resuspended in the media by gentle pipetting and centrifuged for 2 min at 200xg. 8×10^5 hiPSCs
402 were used in 100 μL nucleofector solution per electroporation reaction.

403 Single-stranded DNA oligonucleotide (ssODN) repair template oligos were resuspended in
404 IDTE Buffer (IDT) to a stock concentration of 100 μ M. 1 μ L of ssODN repair template (100 μ M)
405 and 4 μ L of RNP-complex were mixed with the hiPSC solution by gently pipetting, incubated
406 for 5 min at room temperature and transferred to the nucleofection cuvette. Additionally, 1
407 μ L Alt-R Cas9 Enhancer (100 μ M, IDT) was added to the solution to promote transfection
408 efficiency. The nucleofection cuvette was placed in the 4D-Nucleofector (Lonza) and hiPSCs
409 were nucleofected by using the program CA137. After nucleofection, the cuvette was
410 incubated for 5 min under cell culture conditions. Subsequently, hiPSCs were seeded in
411 conditioned medium supplemented with Y-27632 (10 μ M) and bFGF (30 ng/ml)
412 (Supplementary Table 4) on a Matrigel-coated 24-well plate for 72 hours at 37 $^{\circ}$ C.

413 Subcloning and off-target analysis

414 72 hours after nucleofection, hiPSC were dissociated with Accutase and seeded in conditioned
415 medium with Y-27632 (10 μ M) and bFGF (30 ng/ml) at low seeding densities of 100, 250, 750,
416 1000 hiPSCs per well (10 cm^2) in a Matrigel-coated 6-well plate. In addition, the remaining
417 nucleofected hiPSCs were seeded at a higher density of 5×10^5 cells per well (10 cm^2) in a
418 Matrigel-coated 6-well plate. Low-density hiPSC seedings were expanded for 9 to 10 days
419 under daily conditioned medium change until clonal hiPSC colonies reached a size appropriate
420 to pick. HiPSC cultures were incubated with conditioned medium with Y-27632 (10 μ M) for 2
421 hours and sterile 100 μ L-pipette tips were used to carefully scrape individual colonies from
422 the 6-well plate and transfer them to Matrigel-coated 48-well plates into individual wells. 30
423 to 50 clones were picked per transfection approach and were sub-cultivated for 3-4 more days
424 before they reached confluency and were splitted with a ratio of 1:2 into two 48-well copy
425 plates. Colonies were again expanded with daily medium change until they reached
426 confluency. One of the copy plates was used for cryo-preservation, while the second plate was
427 used for DNA isolation. Cryopreservation was performed in 90% FBS and 10% DMSO.

428 QIAcube HT System (Qiagen) and QIAamp 96 DNA QIAcube HT kit (Qiagen) were used for DNA
429 isolation according to the manufacturer's instructions. Cryotubes of successfully edited hiPSC
430 clones were thawed and expanded for master cell bank and working cell bank. Ten most likely
431 off-targets were predicted (*in silico* tool IDT, Custom Alt R CRISPR-Cas9 gRNA software and
432 CRISPOR software). Corresponding PCR primers were designed and PCR products were

433 analysed by 1% (w/v) agarose electrophoresis and Sanger sequencing. Off-target primer
434 sequences can be found in Supplementary Table 6.

435 Karyotyping

436 Karyotype analysis was performed using the nCounter Human Karyotype Panel (Nanostring
437 Technologies) according to the manufacturer's instructions with 250 µg DNA as starting
438 material. The nCounter CNV Collector Tool software (Nanostring) was used for analysis.

439 Cardiac differentiation

440 hiPSC were differentiated into cardiomyocytes with an embryoid body (EB)- and growth
441 factor-based three-stage protocol which was recently described⁵⁴. In brief, hiPSC were
442 expanded on Geltrex-coated T80-flasks to a confluency of 90-100% and detached with EDTA.
443 The formation of EBs was induced in 500 mL spinner flasks with a density of 30-35x10⁶ hiPSCs
444 per 100 mL of EB formation medium (Supplementary Table 4). hiPSC suspension was
445 cultivated overnight at 40 rpm glass ball impeller rotation speed. Mesoderm induction was
446 induced in mesoderm induction medium (Supplementary Table 4) with a volume of 200-300
447 µL EB per pluronic-coated T175-flask for three days under hypoxic conditions (5% O₂) with
448 50% media exchange daily. After washing the EBs again, cardiac differentiation was induced
449 in cardiac differentiation medium 1 (Supplementary Table 4) with a volume of 250-300 µL EBs
450 per pluronic-coated T175-flask with 50% media exchange daily for three days under normoxic
451 conditions (21% O₂). Then, media was completely removed and exchanged for cardiac
452 differentiation medium 2 (Supplementary Table 4). After a daily 50% medium change for four
453 days, culturing medium was exchanged with cardiac differentiation medium 3 (Supplementary
454 Table 4). After washing EBs in HBBS-solution buffer, beating cardiomyocytes were dissociated
455 with collagenase II solution (200 units/mL; Worthington) containing myosin II ATPase inhibitor
456 N-benzyl-p-toluene sulphonamide (BTS) for 2-3 hours until dispersing single cells could be
457 observed. Dissociated hiPSC-CM were frozen in freezing media containing 90% FBS and 10%
458 DMSO or resuspended in EHT casting medium for subsequent EHT generation. Differentiation
459 efficiency (% cTNT-positive cells) was determined by fluorescent-labeled cardiac troponin T
460 (cTNT)- antibody (Miltenyi Biotech) by flow cytometer FACSCanto II (BD). Adjustment of gates
461 adjusted according to the isotype control and performed with FACSDiva software (BD).

462 Differentiation runs with at least 75% cTNT-positive cells were used for further functional
463 experiments. FACS reagents are shown in Supplementary Table 7.

464 Engineered heart tissues (EHT)

465 Engineered heart tissues (EHT) were generated as recently described⁵⁵. In brief, dissociated
466 hiPSC-CM were centrifuged (100xg, 10 minutes) and resuspended in EHT casting medium
467 containing DMEM, horse serum, and glutamine (Supplementary Table 4).
468 Polytetrafluorethylene (PTFE) spacers (EHT Technologies) were placed in a warm 2% (w/v)
469 agarose/PBS solution in a 24-well plate. Agarose solidification at room temperature led to the
470 formation of agarose molds. PTFE spacers were removed from the 24 well plates and flexible
471 polydimethylsiloxane (PDMS) posts were placed on the 24-well plates so that pairs of elastic
472 PDMS posts reached into each casting mold. 100 μ L of the mastermix (Supplementary Table
473 4) containing 2x DMEM, Y-27632, fibrinogen and 1.0×10^6 hiPSC-CMs was resuspended in EHT
474 casting medium, rapidly mixed with 3 μ L thrombin and pipetted into one agarose casting mold.
475 Afterwards the preparation was placed in an incubator for 1.5 hours at 37 °C until a fibrin gel
476 formed in the agarose molds around the PDMS posts. 200-300 μ L of pre-warmed EHT culture
477 medium was added dropwise into each well to ameliorate the detachment of the fibrin gel
478 from the agarose mold. After additional 15-30 minutes of incubation, racks with fibrin gels
479 attached to the PDMS posts were transferred into a new 24-well plate, filled with pre-warmed
480 EHT culture medium, and incubated at 40% O₂, 37 °C, 7% CO₂, and 98% humidity. EHTs were
481 cultured for 28-42 days with medium changes 3 times per week. After 5-7 days of culture,
482 EHTs started to develop spontaneous macroscopic contractions.

483 Video-optical contraction analysis

484 EHT contractile analysis was performed as previously described^{54,55}. EHT contraction
485 parameters, e.g. force, frequency, and contraction kinetics, were monitored over time of EHT
486 development 2 hours after each medium change. EHTs were electrically stimulated as
487 previously described by Hirt et al.⁵⁶. PDMS racks with EHTs were mounted onto custom-made
488 graphite pacing units and stimulated by using Grass S88X Dual Output Square stimulator
489 (Natus Neurology Incorporated). The pacing frequency was adjusted to a value of 1.5 to 2-fold
490 of the spontaneous beating frequency of the EHT batch with an output voltage of 2 V in

491 biphasic pulses of 4 ms. EHTs that were not able to follow the pacing frequency, were excluded
492 from the analysis. Average contraction peaks were calculated with an average of 10-15 peaks.

493 Glucose- and lactate measurement

494 Glucose- and lactate concentrations were measured in EHT cell culture media by blood gas
495 analysis. Samples were collected at baseline and after 24 hours of incubation in EHT medium
496 on day 21 of culture and stored at -20°C. The blood gas analysis instrument ABL90 FLEX
497 Analysator (Radiometer) was used to determine the metabolite concentrations by injecting
498 the supernatant (0.5 mL) into the instrument with a 1 mL syringe.

499 Fatty acid- and carnitine supplementation

500 EHTs were cultured in serum-containing EHT culture medium until force values reached their
501 plateau phase approximately at day 21-28 after generation. Then, EHTs were transferred to a
502 serum- and glucose-free DMEM medium containing linoleic acid- and oleic acid-albumin
503 (Sigma). The detailed serum-free fatty acid medium composition is shown in Supplementary
504 Table 4. Contraction analysis was done daily after 2 hours of medium incubation for 4 days.
505 Supplementation with carnitine was conducted by adding 2 mM L-carnitine hydrochloride
506 (Sigma) to the EHT medium over the entire time of tissue cultivation.

507 Transmission electron microscopy

508 EHTs were transferred into a 24-well plate containing Tyrode's solution (Supplementary
509 Table 4) with 1.8 mM Ca²⁺ and 30 mM butanedione monoxime (BDM) for 3-4 hours until EHTs
510 completely stopped contraction. For fixation, EHTs were shifted into 4% paraformaldehyde
511 (PFA, Thermo Scientific) in 0.1 M phosphate buffer containing 1% glutaraldehyde (Science
512 Services) overnight at 4 °C. Samples were rinsed three times in 0.1 M sodium cacodylate buffer
513 (pH 7.2–7.4) and osmicated using 1% osmium tetroxide in cacodylate buffer. Following
514 osmication, the samples were dehydrated using ascending ethanol concentrations, followed
515 by two rinses in propylene oxide. Infiltration of the embedding medium was performed by
516 immersion in a 1:1 mixture of propylene oxide and Epon (Science Services, Germany), followed
517 by neat Epon and hardening at 60 °C for 48 hours. For light microscopy, semi-thin sections (0.5
518 µm) with longitudinal orientation were mounted on glass slides and stained for 1 minute with
519 1% toluidine blue. For electron microscopy, ultra-thin sections (60 nm) were cut and mounted

520 on copper grids and stained using uranyl acetate and lead citrate. Sections were examined
521 and photographed using an EM902 (Zeiss) electron microscope equipped with a TRS 2K digital
522 camera (A. Tröndle, Moorenweis, Germany).

523 Analysis of acylcarnitines and ceramides

524 EHT cells were homogenized in Milli-Q water (approximately 1.0×10^6 hiPSC-CM per 100 μ l)
525 using the Precellys 24 Homogenisator (Peqlab). The protein content of the homogenate was
526 routinely determined using bicinchoninic acid. Levels of acylcarnitines and ceramides in the
527 cell homogenates were determined by Liquid Chromatography coupled to Electrospray
528 Ionization Tandem Mass Spectrometry (LC-ESI-MS/MS).

529 Acylcarnitines

530 Acylcarnitines were derivatized to butyl esters and using a procedure previously described⁵⁷
531 with several modifications: To 100 μ L of cell homogenate 750 μ L of extraction solution
532 (methanol (containing 0.005% 3,5-di-*tert*-4-butylhydroxytoluol)/Milli-Q water/chloroform
533 4:1:1 (v/v/v)) and 20 μ L of an internal standard mixture, containing deuterated acylcarnitines
534 (Lyophilized Internal Standard MassChrom Amino Acids and Acylcarnitines from Dried Blood,
535 Chromsystems, reconstituted in 2.5 ml, then 1:5 diluted), were added. After thorough mixing
536 and centrifugation (16,100 RCF, 10 min, 4 °C), the supernatant was transferred to a new tube.
537 The residue was re-extracted with 750 μ L of extraction solution. The supernatants were
538 pooled and dried under a stream of nitrogen. The evaporated extracts were treated with 200
539 μ L of freshly prepared derivatization solution (*n*-butanol/acetyl chloride 95:5 (v/v)). After
540 incubation for 20 min at 60 °C in a ThermoMixer (Eppendorf) at 800 rpm, the samples were
541 again dried under nitrogen. After the addition of 100 μ L of methanol/water 3:1 (v/v) and
542 centrifugation (16,100 RCF, 10 min, 4 °C), 80 μ L of supernatant were transferred to
543 autoinjector vials. LC-ESI-MS/MS analysis was performed as previously described⁵⁸. The LC
544 chromatogram peaks of butyl esters of endogenous acylcarnitines and internal standards
545 were integrated using the MultiQuant 3.0.2 software (SCIEX). Endogenous acylcarnitine
546 species were quantified by normalizing their peak areas to the peak area of the internal
547 standards. These normalized peak areas were normalized to the protein content of the
548 sample.

549 Ceramides

550 To 50 μ L of cell homogenate 50 μ L of Milli-Q water, 750 μ L of methanol/chloroform 2:1 (v/v),
551 and internal standard (127 pmol ceramide 12:0, Avanti Polar Lipids) were added. Lipid
552 extraction and LC-ESI-MS/MS analysis were performed as previously described ⁵⁹. The LC
553 chromatogram peaks of endogenous ceramide species and the internal standard ceramide
554 12:0 were integrated using the MultiQuant 3.0.2 software (SCIEX). Endogenous ceramide
555 species were quantified by normalizing their peak areas to the peak area of the internal
556 standard ceramide 12:0. These normalized peak areas were normalized to the protein content
557 of the sample.

558 Actions potential

559 Actions potential (AP) measurements in EHT were performed with standard sharp
560 microelectrode as described previously ⁶⁰. The EHTs were transferred from the 24-well EHT
561 culture plate into the AP measuring chamber by cutting the silicone posts and were fixed with
562 needles in recording chamber. All measurements were done with tissues continuously
563 superfused with Tyrode's solution (NaCl 127 mM, KCl 5.4 mM, MgCl₂ 1.05 mM, CaCl₂ 1.8 mM,
564 glucose 10 mM, NaHCO₃ 22 mM, NaHPO₄ 0.42 mM, balanced with O₂-CO₂ [95:5] at 36 °C, pH
565 7.4). Microelectrodes had a resistance between 25 - 55 M Ω when filled with 2 M KCl. The
566 signals were amplified by a BA-1s npi amplifier (npi electronic GmbH, Tamm, Germany). APs
567 were recorded and analyzed using the Lab-Chart software (version 5, AD Instruments Pty Ltd.,
568 Castle Hill NSW, Australia). Take-of potential (TOP) was defined as the diastolic membrane
569 potential directly before the upstroke.

570 Analysis of mitochondrial respiration

571 The Seahorse™ XF96 extracellular flux analyzer was used to assess mitochondrial respiration
572 as previously described (Mosqueira et al, 2019), using the Mito Stress Kit (Agilent
573 Technologies). Briefly, cryopreserved isogenic sets of hiPSC-CMs were seeded into Matrigel™-
574 coated (BD #356235) XF96 well plates at a density of approximately 5000 cells/mm². HiPSC-
575 CMs were cultured for 2 days in RPMI1640 (USBiological Life Sciences #R9010-01)
576 supplemented with B-27 with insulin (LifeTechnologies #0080085-SA), 2 mM L-glutamine (Life
577 Technologies #25030-081), 10% Fetal Bovine Serum (Gibco #16000044) and 0.6 mM CaCl₂.
578 After 2 weeks, medium was exchanged for XF basal medium (Agilent Technologies #102353),

579 supplemented with 10 mM glucose (Sigma #G7528), 1 mM sodium pyruvate (Sigma #S8636)
580 and 2 mM L-glutamine (Life Technologies #25030-081) 1h before the conduction of the assay.
581 Selective inhibitors were sequentially injected during the measurements (1.5 μ M oligomycin,
582 0.4 μ M FCCP, 1 μ M rotenone; Agilent Technologies), following the manufacturer's
583 instructions. The measured Oxygen Consumption Rate (OCR) values were normalized to the
584 number of cells in each well, quantified by 1:400 Hoechst33342 staining (Sigma #B2261) in
585 PBS (Gibco #14190-094) using fluorescence at 355 nm excitation and 460 nm emission in an
586 automated imaging platform (CellaVista, Syntec).

587 Tandem Mass Tag (TMT)-based quantitative proteomic analysis

588 EHT harvesting for quantitative mass spectrometry

589 EHTs from hiPSC-CMs were cultured in EHT medium for 28 days before proteome analysis.
590 EHTs were washed twice in warm PBS buffer and incubated with collagenase II solution
591 (collagenase II (200 units per mL), HBSS minus $\text{Ca}^{2+}/\text{Mg}^{2+}$, HEPES (10 mM), Y-27632 (10 μ M),
592 and BTS (30 μ M)) in a falcon tube for 3 hours. Dissociated hiPSC-CMs were gently titrated with
593 a 1000 μ L-pipette (Eppendorf) until the last cluster of cells was disaggregated, spun down for
594 5 min at 200xg and supernatant was removed. The pellet was frozen in liquid nitrogen and
595 stored at -80 $^{\circ}$ C before subjection to quantitative proteome analysis.

596 Tissue protein extraction and digestion for mass spectrometry

597 Cell pellets were lysed in 50 mM Tris, 0.1% SDS, pH=8.8, with protease inhibitors. After
598 centrifugation at 4 $^{\circ}$ C at 16,000xg for 10 min, the supernatant was transferred to new 1.5 mL
599 tubes and protein concentration was measured using a BCA protein assay kit (Thermo Fisher
600 Scientific). For each sample, 23 μ g of proteins were denatured by the addition of 9 M urea,
601 3 M thiourea (final conc. 6 M urea, 2 M thiourea) and reduced by the addition of 100 mM DTT
602 (final conc. 10 mM) followed by incubation at 37 $^{\circ}$ C for 1 hour, 240 rpm. The samples were
603 then alkylated by the addition of 500 mM iodoacetamide (final conc. 50 mM) followed by
604 incubation in the dark for 1h at room temperature. Pre-chilled (-20 $^{\circ}$ C) acetone (1:9 volume
605 ratio) was used to precipitate the samples overnight at -20 $^{\circ}$ C. Samples were centrifuged at
606 16,000xg for 30 min at 4 $^{\circ}$ C and the supernatant was subsequently discarded. Protein pellets
607 were dried using a vacuum centrifuge (Thermo Fisher Scientific, Savant SPD131DDA), re-
608 suspended in 0.1M TEAB buffer, pH 8.2 (Sigma T7408), and 0.6 μ g trypsin was added. The

609 digestion was performed overnight at 37 °C, 240 rpm, and stopped by adding 10% TFA (final
610 conc. 1%). C18 clean-up was performed using Agilent Bravo AssayMAP and the eluted peptides
611 were dried using a vacuum centrifuge.

612 Sample labeling for mass spectrometry

613 The samples were resuspended in 0.1 M TEAB and a pooled sample was made by taking the
614 same amount of proteins from each individual sample. Samples were labeled with Tandem
615 Mass Tag (TMT) 11-plex reagent (Thermo Fisher Scientific) following the manufacturer's
616 instructions. The pooled sample labeled with TMT-126 was used as an internal standard. The
617 samples labeled with different tags of the 11-plex TMT were combined, dried, and
618 resuspended in 300 µl of 0.1% TEA. Samples were further fractionated using high pH RP HPLC
619 (Agilent 300Extend-C18 3.5µm 4.6x150mm P/N 763973-902) and 16 fractions were collected
620 for each TMT mixture. All fractions were dried and resuspended in LC solution (2% acetonitrile
621 (ACN), 0.05% TFA).

622 Mass spectrometry analysis

623 Samples were injected and separated by a nanoflow HPLC (Ultimate 3000 RSLCnano, Thermo
624 Fisher Scientific) on an EASY-Spray column (C18, 75 µm x 50 cm, 2 µm) using 2 hour LC
625 gradient: 0-10 min, 4%-10%B; 10-75 min, 10%-30%B; 75-80 min, 30%-40%B; 80-85 min, 40%-
626 99%B; 85-90 min, 99%B; 90-120 min, 4%B; A=0.1% FA in H₂O and B= 0.1% FA, 80% ACN in
627 H₂O. The flow rate was 250 nl/min and column temperature was set at 45°C. The separated
628 peptides were directly injected to an Orbitrap Fusion Lumos MS (Thermo Fisher Scientific) and
629 analyzed using a synchronous precursor selection (SPS)-based MS³ method for TMT-labeled
630 sample. Full MS spectra were collected on the Orbitrap with a resolution of 120,000 and scan
631 range 375-1500 m/z. The most abundant ions were fragmented using CID and MS² spectra
632 were collected on a linear ion trap, with dynamic exclusion enabled. The 5 most abundant ions
633 from every MS² spectrum were selected and fragmented at the same time using HCD with
634 collision energy 65% and MS³ spectra were collected on the Orbitrap with a resolution of
635 60,000 and a scan range of 110-500 m/z to measure the TMT reporter ions. The cycle time
636 was set at 3 seconds.

637 Raw data were analyzed using Proteome Discoverer 2.4. The 16 fractions of each TMT
638 mixtures were loaded as fractions and analyzed together. Each TMT tag was assigned to the

639 correct sample and group. Data were searched against the human UniProt/SwissProt database
640 (version 2020_01, 20365 protein entries). Trypsin was used as an enzyme and maximum 2
641 missed cleavage was allowed. The precursor mass tolerance was set at 10 ppm and fragment
642 mass tolerance was set at 0.8 Da. Carbamidomethylation on cysteine and TMT 6plex on N-
643 terminal and lysine were used as static modifications. Oxidation on methionine was used as a
644 dynamic modification. Reporter ions S/N were used for quantification. The quantification
645 values were normalized to total peptide amount and scaled on controls (pooled sample
646 labeled with TMT-126). The scaled abundance was exported for further analysis.

647 The dataset was first imputed to replace missing relative quantities to zeros when these were
648 consistent among any of the examined phenotypes. In specific, when the percent of missing
649 values in one examined phenotype exceeded 90% and the percentage of missing values for
650 the other phenotypes was below 10% then the missing values of the examined phenotype
651 were imputed to zeros. The relative quantities of the proteins were then scaled using log2
652 transformation. Next, the dataset was filtered to keep only proteins with less than 30% missing
653 values, without considering the previously imputed missing values as missing. The remaining
654 missing values were imputed using KNN-Impute method with k equal to 3. The limma package
655 has been used to compare different phenotypes using the Ebayes algorithm and correcting for
656 selected covariates. The initial p-values were adjusted for multiple testing using Benjamini-
657 Hochberg method and a threshold of 0.05 was used for the adjusted p-values to infer
658 statistically significant changes.

659 Pathway enrichment analysis of significant proteins

660 The bioinformatic webtool Webgestalt⁶¹ was used for pathway enrichment analysis of KEGG
661 terms. KEGG pathways of significantly enriched proteins (fold change ≥ 1.4) were inferred by
662 Benjamini-Hochberg testing with a p-value threshold of 0.05 and a maximum number of 150
663 proteins per category. To visualize the samples based on their proteomic profiles, principal
664 component analysis (PCA) was conducted, and samples were projected in a 2D space based
665 on their 2 most significant principal components. Samples were color-coded based on their
666 phenotype. Volcano plots for the visualization of differentially expressed proteins were
667 generated in GraphPad PRISM.

668 Gene expression analysis, mitochondrial DNA quantification

669 Total RNA was extracted from samples and complementary DNA (cDNA) was generated by
670 reverse transcription using the TRIzol and high-capacity cDNA reverse transcription kit
671 (Applied Biosystems) according to the manufacturer's instructions. All experiments were
672 performed using technical triplicates. The $\Delta\Delta\text{Ct}$ method was used for calculation of relative
673 transcript expression levels. Primer sequences are listed in Supplementary Table 8. Gene
674 expression of target genes was normalized to the reference transcripts of the housekeeping
675 gene glucuronidase-beta (GUSB). The qPCR experiments were conducted with the AbiPrism
676 7900HT Fast Real-Time PCR System (Applied Biosystems) using HOT FIREPol EvaGreen qPCR
677 Mix Plus (Solis BioDyne).

678 Quantification of mitochondrial DNA (mtDNA) was performed according to a qPCR protocol
679 recently described by Ulmer et al.⁶². In brief, genomic DNA (including mitochondrial DNA) was
680 isolated by TRIzol extraction according to the manufacturer's instruction. DNA concentrations
681 of each sample was adjusted to 16.5 $\mu\text{g}/\mu\text{L}$ prior to the experiment by dilution. The mt-DNA
682 content was quantified by normalizing gene expression values of the mitochondrially encoded
683 NADH dehydrogenase- 1 (mt-ND1) and -2 (mt-ND2) to the nuclear-encoded globular actin (g-
684 actin). Primer sequences were used as described^{62,63} and are listed in Supplementary table 8.

685 Southern blot

686 Southern blot probe design.

687 The 5'HR probe was cloned using PCR primer pairs SLC_5HR1 (Supplementary Table 9), and
688 PCR amplified using pairs SLC_5HR2. The 3'HR probe was cloned using PCR primer pairs
689 SLC_3HR1, and PCR amplified using pairs SLC_3HR2 (Supplementary Table 9).

690 The Southern blot procedure was performed according to Skryabin et al.⁶⁴. HiPSC were
691 thawed from an MCB aliquot and expanded to T25 flask format with 100% confluency. HiPSCs
692 were washed with 5 mL PBS per flask and lysed in 1 mL standard lysis buffer containing 100
693 mM Tris-HCl (pH 8.5), 5 mM EDTA, 0.2% SDS, 200 mM NaCl, 100 g/mL Proteinase K (Roche)
694 incubated overnight at 37 °C. DNA was extracted by phenol, phenol/chloroform extraction,
695 precipitated in isopropanol and washed in 80% ethanol. DNA samples were dissolved in TE
696 buffer. Approximately 10-15 μg of genomic DNA was digested with *EcoRI*, and *HindIII*

697 restriction endonucleases, fractionated on 0.8% agarose gels and transferred to GeneScreen
698 nylon membranes (NEN DuPont, USA). The membranes were hybridized with a ³²P-labeled
699 0,5-kb 5'HR probe containing sequences 5' to the deleted region (5'HR probe, Supplementary
700 Figure 3) and washed with SSPE buffer (0.09 M NaCl, 5 mM NaH₂PO₄, and 0.5 mM EDTA [pH
701 7.7]) and 0.5% sodium dodecyl sulfate at 65°C. Similarly, membranes were hybridized and
702 washed with a ³²P-labeled 1,2-kb 3'HR probe containing sequences 3' to the deleted region
703 (3'HR probe, Supplementary Figure 3).

704 Single-nucleus RNA sequencing

705 EHTs were washed with PBS, detached from the PDMS posts, frozen in liquid nitrogen, and
706 stored at -150 °C. Single-nucleus RNA sequencing (snRNA seq) was performed according to
707 Litviňuková et al. ⁶⁵. In brief, single nuclei were isolated from frozen EHTs and purified by
708 fluorescent-activated cell sorting (FACS). Nuclei were further processed using the Chromium
709 Controller (10X Genomics) according to the manufacturer's protocol with a targeted nuclei
710 recovery of 5,000 per reaction. 3' gene expression libraries were prepared according to the
711 manufacturer's instructions of v3 Chromium Single Cell Reagent Kits (10X Genomics).

712 Sequencing data analysis

713 Bcl files were converted to Fastq files by using bcl2fastq. Each sample was mapped to the
714 human reference genome GRCh38 (release Ens84) using the CellRanger suite (v.3.0.1).
715 Mapping quality was assessed using the cellranger summary statistics; Empty droplets were
716 identified by Emptydrops, implemented in the CellRanger workflow, and subsequently
717 removed, while doublets were identified and filtered using Solo ⁶⁶.

718 Downstream analysis was performed using the Python Scanpy v1.5.1 toolkit. Single nuclei
719 were filtered for counts ($300 \leq n_counts \leq 20,000$), genes ($500 \leq n_genes \leq 5,500$),
720 mitochondrial genes ($percent_mito \leq 1\%$), ribosomal genes ($percent_ribo \leq 1\%$), and soft max
721 score detected by Solo ($solo_softmax_scores \leq 0.5$). After read count normalization and log-
722 transformation, highly variable genes were selected. Principal components were computed,
723 and elbow plots were used to define the appropriate number of principal components for
724 neighbor graph construction. Prior to manifold construction using UMAP, selected principal
725 components were harmonized by using Python Harmony. Finally, nuclei were clustered
726 using the network-based Leiden algorithm.

727 Statistical analysis

728 GraphPad Prism software 8.4.3 was used to perform statistical analysis. All data was depicted
729 as mean±SEM either as scatterplots or bar graphs. Where possible, data sets were tested for
730 normal distribution and the appropriate statistical test was chosen accordingly. Either the
731 unpaired or nested Student's t-test, a nested-, a classical one-way ANOVA or a two-way
732 ANOVA (plus Bonferroni's post-test) was used to determine whether the difference between
733 groups was statistically significant. A p-value lower than 0.05 was statistically significant.

734 References

- 735 1. Longo, N., Frigeni, M. & Pasquali, M. Carnitine transport and fatty acid oxidation.
736 *Biochim. Biophys. Acta - Mol. Cell Res.* **1863**, 2422–2435 (2016).
- 737 2. Wagner, C. A. *et al.* Functional and pharmacological characterization of human Na⁺-
738 carnitine cotransporter hOCTN2. *Am. J. Physiol. - Ren. Physiol.* **279**, (2000).
- 739 3. Wu, X., Prasad, P. D., Leibach, F. H. & Ganapathy, V. cDNA Sequence, Transport
740 Function, and Genomic Organization of Human OCTN2, a New Member of the Organic
741 Cation Transporter Family. *Biochem. Biophys. Res. Commun.* **246**, 589–595 (1998).
- 742 4. Tamai, I. *et al.* Molecular and functional identification of sodium ion-dependent, high
743 affinity human carnitine transporter OCTN2. *J. Biol. Chem.* **273**, 20378–20382 (1998).
- 744 5. Cooper, D. E., Young, P. A., Klett, E. L. & Coleman, R. A. Physiological consequences of
745 compartmentalized acyl-CoA metabolism. *J. Biol. Chem.* **290**, 20023–20031 (2015).
- 746 6. Wang, S. S., Rao, J., Li, Y. F., Zhang, Z. W. & Zeng, G. H. Primary carnitine deficiency
747 cardiomyopathy. *Int. J. Cardiol.* **174**, 171–173 (2014).
- 748 7. Magoulas, P. L. & El-Hattab, A. W. Systemic primary carnitine deficiency: An overview
749 of clinical manifestations, diagnosis, and management. *Orphanet Journal of Rare*
750 *Diseases* vol. 7 (2012).
- 751 8. Longo, N., Amat Di San Filippo, C., Pasquali, M., Filippo, C. A. di S. & Pasquali, M.
752 Disorders of carnitine transport and the carnitine cycle. *Am. J. Med. Genet. - Semin.*
753 *Med. Genet.* **142 C**, 77–85 (2006).
- 754 9. Rasmussen, J. *et al.* Carnitine levels in 26,462 individuals from the nationwide
755 screening program for primary carnitine deficiency in the Faroe Islands. *J. Inherit.*
756 *Metab. Dis.* **37**, 215–222 (2014).
- 757 10. Alesci, S. *et al.* Carnitine: Lessons from one hundred years of research. *Ann. N. Y.*
758 *Acad. Sci.* **1033**, (2004).
- 759 11. Koeth, R. A. *et al.* Intestinal microbiota metabolism of l-carnitine, a nutrient in red
760 meat, promotes atherosclerosis. *Nat. Med.* **19**, 576–585 (2013).
- 761 12. Rebouche, C. J. Kinetics, pharmacokinetics, and regulation of L-carnitine and acetyl-L-

- 762 carnitine metabolism. *Ann. N. Y. Acad. Sci.* **1033**, 30–41 (2004).
- 763 13. Spiekerkoetter, U. *et al.* Silent and symptomatic primary carnitine deficiency within
764 the same family due to identical mutations in the organic cation/carnitine transporter
765 OCTN2. *J. Inherit. Metab. Dis.* **26**, 613–615 (2003).
- 766 14. Rasmussen, J. *et al.* Increased risk of sudden death in untreated primary carnitine
767 deficiency. *J. Inherit. Metab. Dis.* **43**, 290–296 (2020).
- 768 15. Wilcken, B., Wiley, V., Hammond, J. & Carpenter, K. Screening Newborns for Inborn
769 Errors of Metabolism by Tandem Mass Spectrometry. *N. Engl. J. Med.* **348**, 2304–2312
770 (2003).
- 771 16. Lin, Y. *et al.* Increased detection of primary carnitine deficiency through second-tier
772 newborn genetic screening. *Orphanet J. Rare Dis.* **16**, 1–7 (2021).
- 773 17. Yang, X. *et al.* Newborn Screening and Genetic Analysis Identify Six Novel Genetic
774 Variants for Primary Carnitine Deficiency in Ningbo Area, China. *Front. Genet.* **12**, 1–8
775 (2021).
- 776 18. Tan, J. *et al.* Lifetime risk of autosomal recessive mitochondrial disorders calculated
777 from genetic databases. *EBioMedicine* **54**, 102730 (2020).
- 778 19. Li, F. Y. *et al.* Molecular spectrum of SLC22A5 (OCTN2) gene mutations detected in 143
779 subjects evaluated for systemic carnitine deficiency. *Hum. Mutat.* **31**, (2010).
- 780 20. Tomomura, M. *et al.* Abnormal expression of urea cycle enzyme genes in juvenile
781 visceral steatosis (jvs) mice. *Biochim. Biophys. Acta - Mol. Basis Dis.* **1138**, 167–171
782 (1992).
- 783 21. Koizumi, T., Nikaido, H., Nonomura, A. & Yoneda, T. Infantile disease with
784 microvesicular fatty infiltration of viscera spontaneously occurring in the C3H-H-2°
785 strain of mouse with similarities to Reye's syndrome. *Lab. Anim.* **22**, 83–87 (1988).
- 786 22. Horiuchi, M. *et al.* Cardiac hypertrophy in juvenile visceral steatosis (jvs) mice with
787 systemic carnitine deficiency. *FEBS Lett.* **326**, 267–271 (1993).
- 788 23. Saburi, Y. *et al.* Changes in distinct species of 1,2-diacylglycerol in cardiac hypertrophy
789 due to energy metabolic disorder. *Cardiovasc. Res.* **57**, 92–100 (2003).

- 790 24. Asai, T. *et al.* Combined therapy with PPAR α agonist and l-carnitine rescues lipotoxic
791 cardiomyopathy due to systemic carnitine deficiency. *Cardiovasc. Res.* **70**, 566–577
792 (2006).
- 793 25. Horiuchi, M., Kobayashi, K., Masuda, M., Terazono, H. & Saheki, T. Pyruvate
794 dehydrogenase kinase 4 mRNA is increased in the hypertrophied ventricles of
795 carnitine-deficient juvenile visceral steatosis (JVS) mice. *BioFactors* **10**, 301–309
796 (1999).
- 797 26. Spaniol, M. *et al.* Development and characterization of an animal model of carnitine
798 deficiency. *Eur. J. Biochem* **268**, 1876–1887 (2001).
- 799 27. Liepinsh, E. *et al.* Effects of Long-Term Mildronate Treatment on Cardiac and Liver
800 Functions in Rats. *Basic Clin. Pharmacol. Toxicol.* **105**, 387–394 (2009).
- 801 28. Degrace, P. *et al.* Fatty acid oxidation and related gene expression in heart depleted of
802 carnitine by mildronate treatment in the rat. *Mol. Cell. Biochem.* **258**, 171–182 (2004).
- 803 29. Steuerwald, U. *et al.* Neonatal screening for primary carnitine deficiency: Lessons
804 learned from the Faroe Islands. *Int. J. Neonatal Screen.* **3**, 1–10 (2017).
- 805 30. Chen, X., Kang, R., Kroemer, G. & Tang, D. Broadening horizons: the role of ferroptosis
806 in cancer. *Nat. Rev. Clin. Oncol.* **18**, 280–296 (2021).
- 807 31. Doll, S. *et al.* ACSL4 dictates ferroptosis sensitivity by shaping cellular lipid
808 composition. *Nat. Chem. Biol.* **13**, 91–98 (2017).
- 809 32. Li, D. & Li, Y. The interaction between ferroptosis and lipid metabolism in cancer.
810 *Signal Transduct. Target. Ther.* **5**, 1–10 (2020).
- 811 33. Zhang, B. *et al.* Liproxstatin-1 attenuates unilateral ureteral obstruction-induced renal
812 fibrosis by inhibiting renal tubular epithelial cells ferroptosis. *Cell Death Dis.* **12**, 1–10
813 (2021).
- 814 34. Gong, Y., Wang, N., Liu, N. & Dong, H. Lipid Peroxidation and GPX4 Inhibition Are
815 Common Causes for Myofibroblast Differentiation and Ferroptosis. *DNA Cell Biol.* **38**,
816 725–733 (2019).
- 817 35. Liu, Q. *et al.* Genome-Wide Temporal Profiling of Transcriptome and Open Chromatin

- 818 of Early Cardiomyocyte Differentiation Derived from hiPSCs and hESCs. *Circ. Res.* **121**,
819 376–391 (2017).
- 820 36. Gélinas, R., Leach, E., Horvath, G. & Laksman, Z. Molecular Autopsy Implicates Primary
821 Carnitine Deficiency in Sudden Unexplained Death and Reversible Short QT Syndrome.
822 *Can. J. Cardiol.* **35**, 1256.e1-1256.e2 (2019).
- 823 37. Roussel, J. *et al.* Carnitine deficiency induces a short QT syndrome. *Heart Rhythm* **13**,
824 165–174 (2016).
- 825 38. Jalil, M. A. *et al.* Attenuation of cardiac hypertrophy in carnitine-deficient juvenile
826 visceral steatosis (JVS) mice achieved by lowering dietary lipid. *J. Biochem.* **139**, 263–
827 270 (2006).
- 828 39. Liepinsh, E. *et al.* Mildronate decreases carnitine availability and up-regulates glucose
829 uptake and related gene expression in the mouse heart. *Life Sci.* **83**, 613–619 (2008).
- 830 40. Li, J. M. *et al.* Systemic regulation of L-carnitine in nutritional metabolism in zebrafish,
831 *Danio rerio*. *Sci. Rep.* **7**, (2017).
- 832 41. Kolwicz, S. C. & Tian, R. Glucose metabolism and cardiac hypertrophy. *Cardiovasc. Res.*
833 **90**, 194–201 (2011).
- 834 42. MacEyka, M. & Spiegel, S. Sphingolipid metabolites in inflammatory disease. *Nature*
835 **510**, 58–67 (2014).
- 836 43. Bandet, C. L. & Hajduch, E. CERT-Dependent Ceramide Transport, A Crucial Process in
837 Cells. *J. Diabetes Clin. Res.* **3**, 40–45 (2021).
- 838 44. Wu, J. & Corr, P. B. Palmitoyl transient carnitine modifies sodium currents and induces
839 inward current in ventricular myocytes. *Am. J. Physiol.* **266**, 1034–1046. (1994).
- 840 45. Wu, J. & Corr, P. B. Palmitoylcarnitine transient inward increases [Na⁺]_i and initiates
841 current in adult ventricular myocytes. *Am. J. Physiol.* **268**, 2405–2417 (1995).
- 842 46. Chaffin, M. *et al.* Single-nucleus profiling of human dilated and hypertrophic
843 cardiomyopathy. *Nature* (2022) doi:10.1038/s41586-022-04817-8.
- 844 47. Nicin, L. *et al.* Single Nuclei Sequencing Reveals Novel Insights into the Regulation of
845 Cellular Signatures in Children with Dilated Cardiomyopathy. *Circulation* 1704–1719

- 846 (2021) doi:10.1161/CIRCULATIONAHA.120.051391.
- 847 48. Tomlinson, S., Atherton, J. & Prasad, S. Primary Carnitine Deficiency: A Rare,
848 Reversible Metabolic Cardiomyopathy. *Case Reports Cardiol.* **2018**, 1–3 (2018).
- 849 49. Grünert, S. C. *et al.* Primary carnitine deficiency-diagnosis after heart transplantation:
850 Better late than never! *Orphanet J. Rare Dis.* **15**, 4–9 (2020).
- 851 50. Yang, W. S. *et al.* Peroxidation of polyunsaturated fatty acids by lipoxygenases drives
852 ferroptosis. *Proc. Natl. Acad. Sci. U. S. A.* **113**, E4966–E4975 (2016).
- 853 51. Doll, S. *et al.* ACSL4 dictates ferroptosis sensitivity by shaping cellular lipid
854 composition. *Nat. Chem. Biol.* **13**, 91–98 (2017).
- 855 52. Shibamiya, A. *et al.* Cell Banking of hiPSCs: A Practical Guide to Cryopreservation and
856 Quality Control in Basic Research. *Curr. Protoc. Stem Cell Biol.* **55**, 1–26 (2020).
- 857 53. Concordet, J. P. & Haeussler, M. CRISPOR: Intuitive guide selection for CRISPR/Cas9
858 genome editing experiments and screens. *Nucleic Acids Res.* **46**, W242–W245 (2018).
- 859 54. Breckwoldt, K. *et al.* Differentiation of cardiomyocytes and generation of human
860 engineered heart tissue. *Nat. Protoc.* **12**, 1177–1197 (2017).
- 861 55. Mannhardt, I. *et al.* Human Engineered Heart Tissue: Analysis of Contractile Force.
862 *Stem Cell Reports* **7**, 29–42 (2016).
- 863 56. Hirt, M. N. *et al.* Functional improvement and maturation of rat and human
864 engineered heart tissue by chronic electrical stimulation. *J. Mol. Cell. Cardiol.* **74**, 151–
865 161 (2014).
- 866 57. Giesbertz, P., Ecker, J., Haag, A., Spanier, B. & Daniel, H. An LC-MS/MS method to
867 quantify acylcarnitine species including isomeric and odd-numbered forms in plasma
868 and tissues. *J. Lipid Res.* **56**, 2029–2039 (2015).
- 869 58. Aravamudhan, S. *et al.* Phosphoproteomics of the developing heart identifies PERM1 -
870 An outer mitochondrial membrane protein. *J. Mol. Cell. Cardiol.* **154**, 41–59 (2021).
- 871 59. Schwamb, J. *et al.* B-cell receptor triggers drug sensitivity of primary CLL cells by
872 controlling glucosylation of ceramides. *Blood* **120**, 3978–3985 (2012).
- 873 60. Lemoine, M. D. *et al.* Human Induced Pluripotent Stem Cell-Derived Engineered Heart

- 874 Tissue as a Sensitive Test System for QT Prolongation and Arrhythmic Triggers. *Circ.*
875 *Arrhythmia Electrophysiol.* **11**, 1–15 (2018).
- 876 61. Liao, Y., Wang, J., Jaehnig, E. J., Shi, Z. & Zhang, B. WebGestalt 2019: gene set analysis
877 toolkit with revamped UIs and APIs. *Nucleic Acids Res.* **47**, W199–W205 (2019).
- 878 62. Ulmer, B. M. *et al.* Contractile Work Contributes to Maturation of Energy Metabolism
879 in hiPSC-Derived Cardiomyocytes. *Stem Cell Reports* **10**, 834–847 (2018).
- 880 63. Burkart, A. M. *et al.* Insulin Resistance in Human iPS Cells Reduces Mitochondrial Size
881 and Function. *Sci. Rep.* **6**, 1–12 (2016).
- 882 64. Skryabin, B. V. *et al.* Pervasive head-to-tail insertions of DNA templates mask desired
883 CRISPR-Cas9-mediated genome editing events. *Sci. Adv.* **6**, (2020).
- 884 65. Litviňuková, M. *et al.* Cells of the adult human heart. *Nature* **588**, 466–472 (2020).
- 885 66. Bernstein, N. J. *et al.* Solo: Doublet Identification in Single-Cell RNA-Seq via Semi-
886 Supervised Deep Learning. *Cell Syst.* **11**, 95-101.e5 (2020).

887

888

889 Acknowledgements

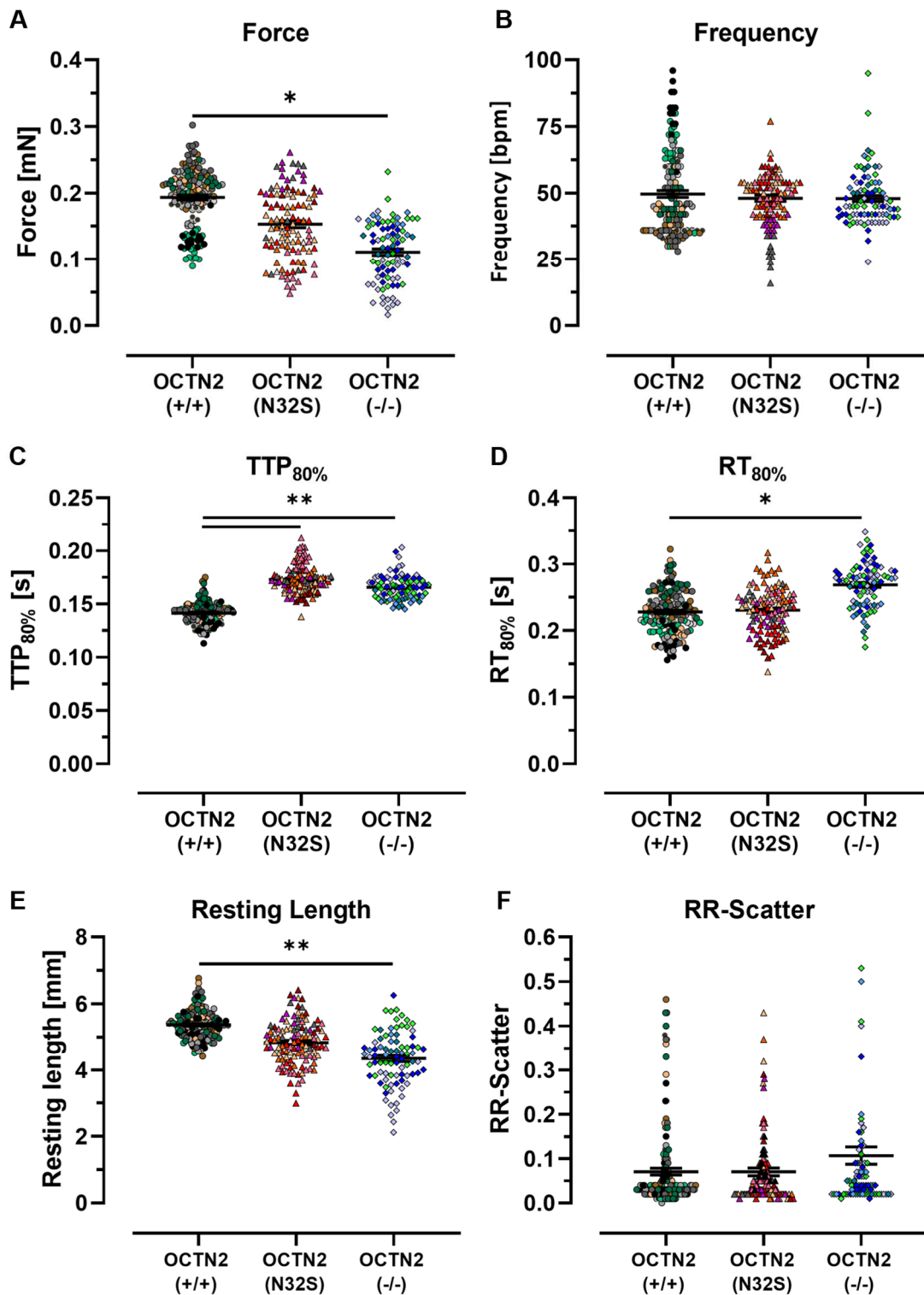
890 We greatly appreciate the assistance of the UKE FACS Core unit, the team approach of hiPSC-
891 and CRISPR/cas9 group at IEPT/UKE and the technical assistance of Anna Steenpaß. This study
892 was supported by the European Research Council (ERC-AG IndivuHeart), Deutsche
893 Forschungsgemeinschaft (DFG Es 88/12-1, DFG HA 3423/5-1), the German Ministry of
894 Education and Research (BMBF) and the Centre for Cardiovascular Research (DZHK), and the
895 Freie und Hansestadt Hamburg. M. Mayr is a British Heart Foundation (BHF) Chair Holder
896 (CH/16/3/32406) with BHF programme grant support (RG/16/14/32397) and is part of the
897 Marie Skłodowska-Curie Innovative Training Network TRAIN-HEART (<http://train-heart.eu>).

898 Author contribution

899 CRISPR/Cas9 (M.L., C.B., B.M.U.), Southern blot (B.V.S., T.S.R.), PCR (M.L.), cardiac
900 differentiation (M.L., B.K., T.S.), EHT generation and maintenance (M.L., B.K., T.S.), force
901 measurement (M.L.), action potential (C.S., T.C.), proteomics/bioinformatics (M.M., K.T., X.Y.,
902 M.L.), single nuclear RNA sequencing (TD.v.B., E.A., H.M., N.H.), lipid analysis (S.B.), mt DNA-,
903 quantitative PCR (M.L.), TEM (M.S.), Seahorse (S.B., C.D.), concept (A.H. M.L., T.E.), funding
904 (T.E., A.H.), writing (M.L., T.E., A.H.)

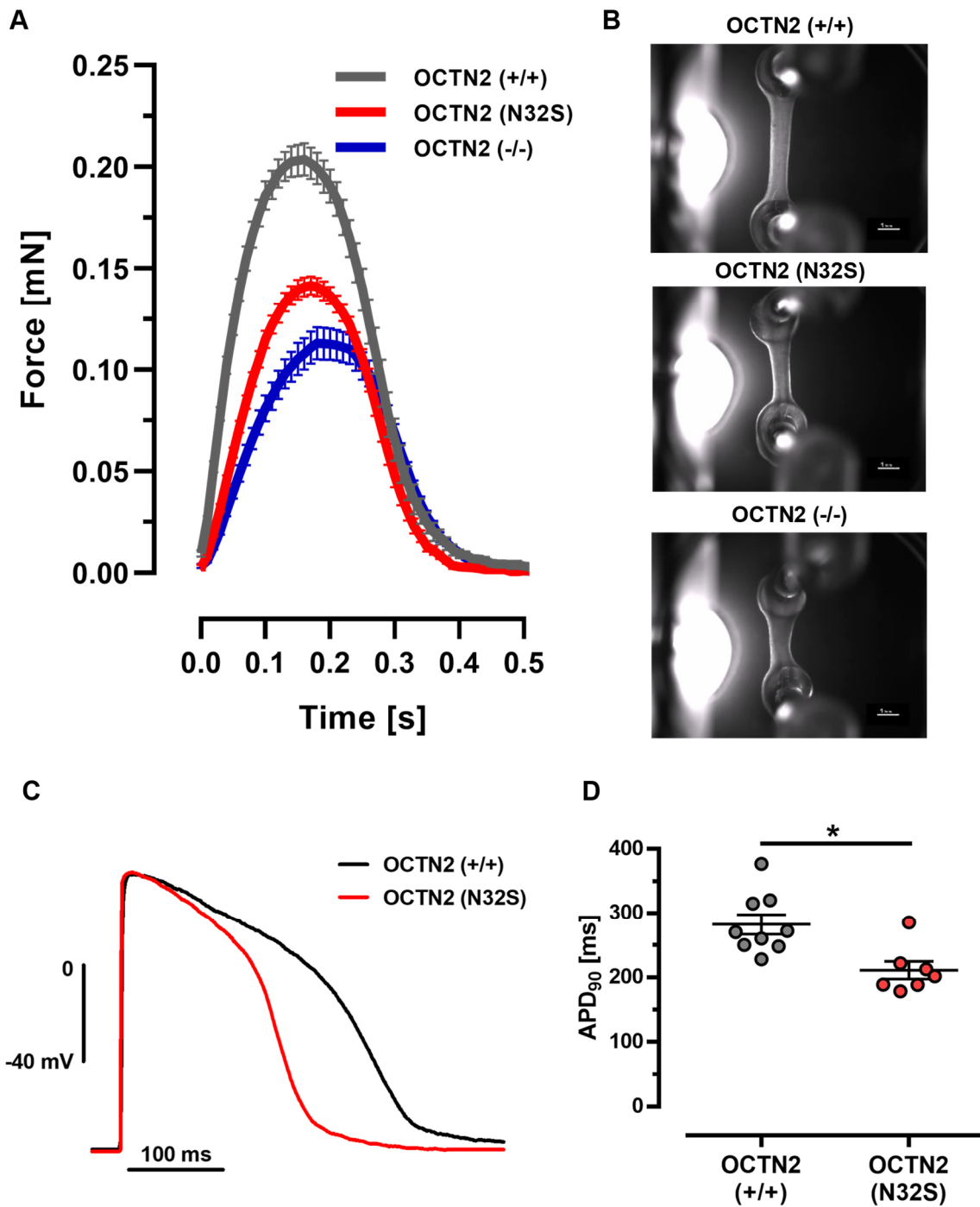
905 Competing interests

906 T.E. is a member of the DiNAQOR Scientific Advisory Board and holds shares in DiNAQOR.



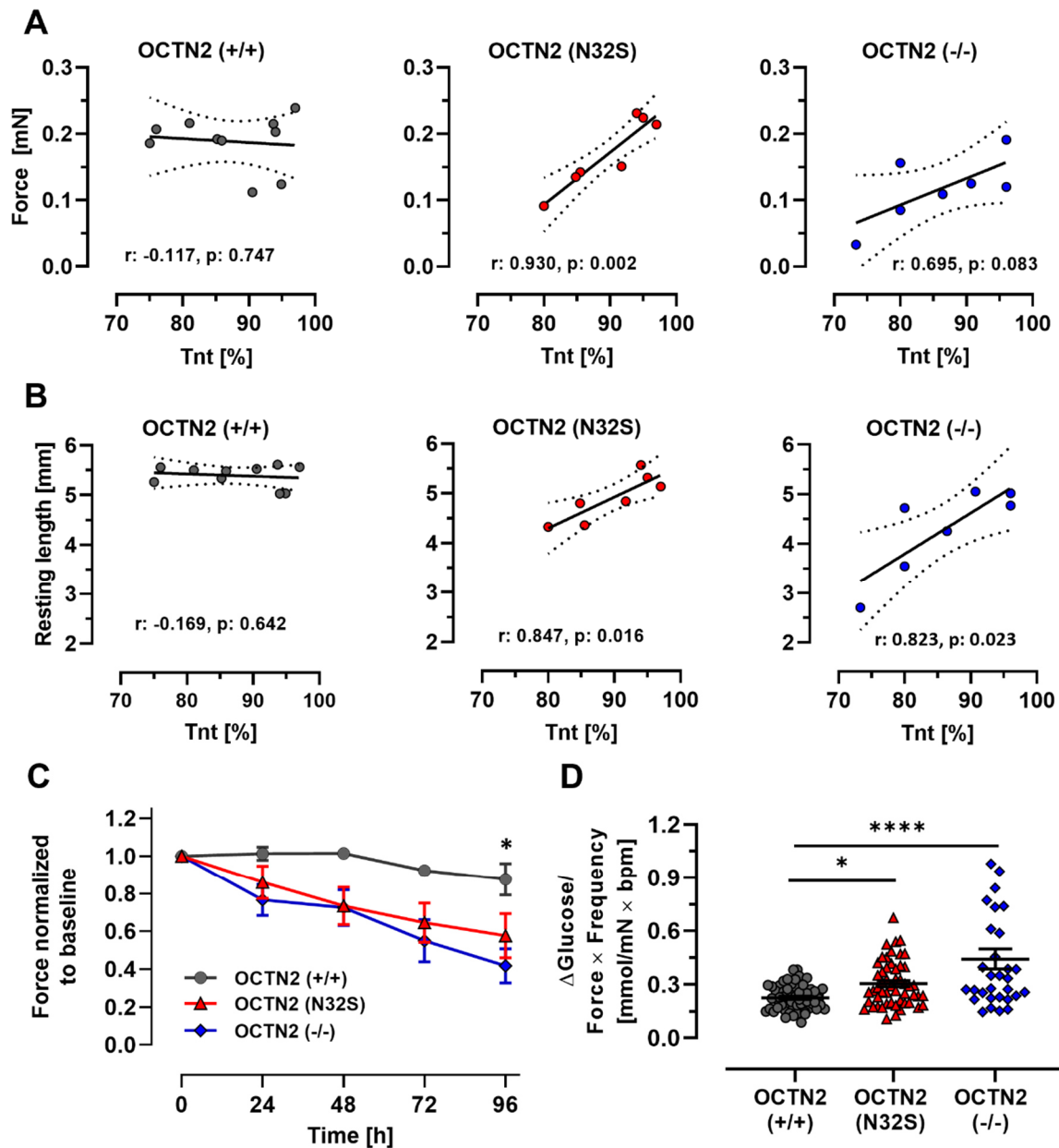
908

909 **Figure 1. A-F: Effect of OCTN2 genotype on contractile parameters of spontaneous beating**
 910 **EHTs on day 21.** OCTN2 (+/+): n=153 EHTs from 9 batches, OCTN2 (N32S): n=108 EHTs from 7
 911 batches, OCTN2 (-/-): n=91 EHTs from 5 batches. Nested 1-way ANOVA followed by
 912 Bonferroni's post-test for multiple comparisons, *p<0.05, **p<0.01, ***p<0.001,
 913 ****p<0.0001. Each data point represents one EHT. Each color represents one independent
 914 differentiation batch. Data are expressed as mean±SEM.

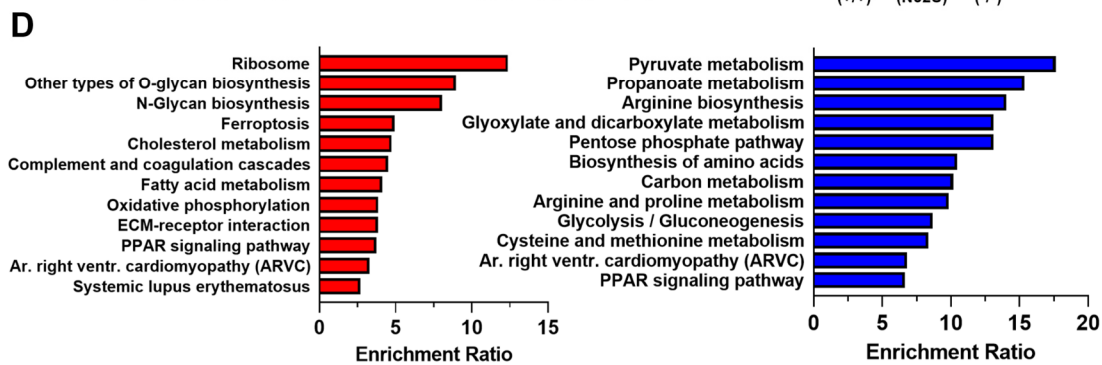
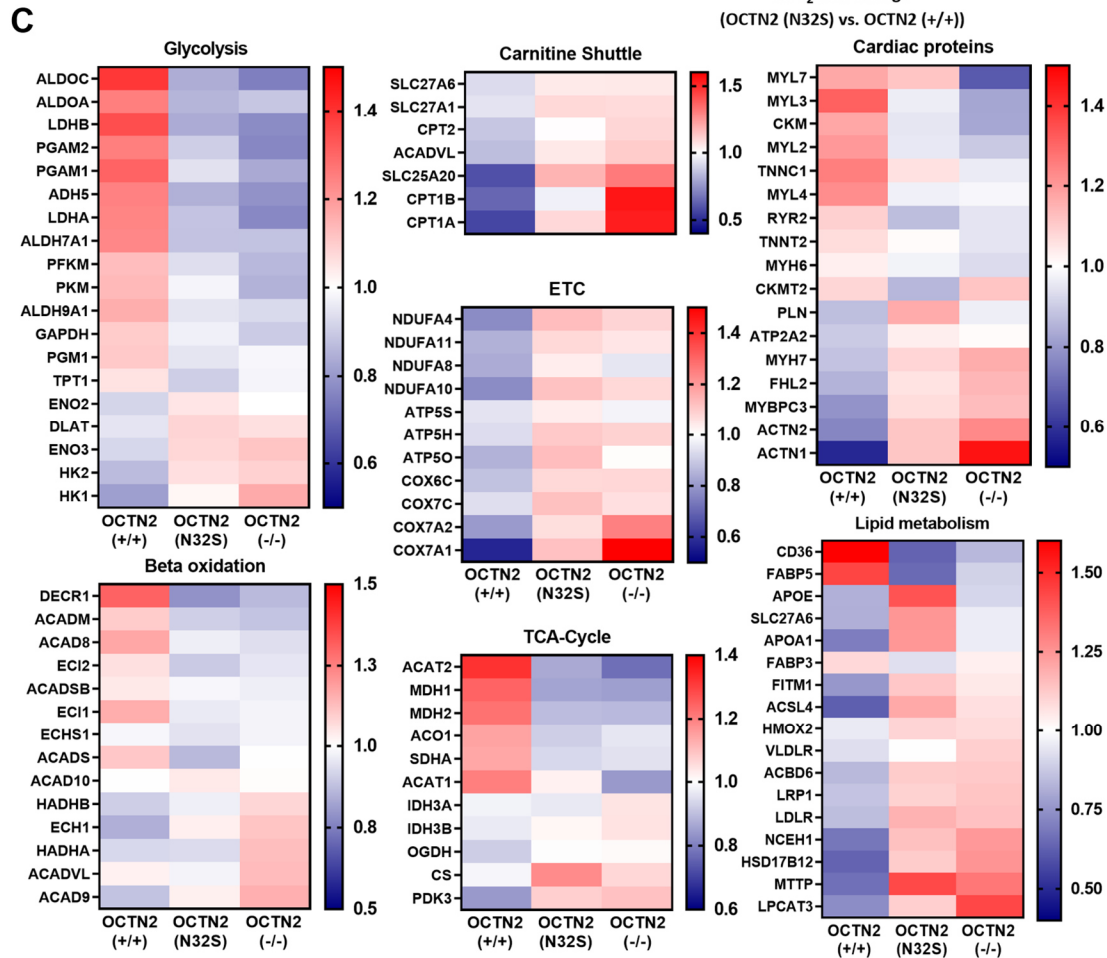
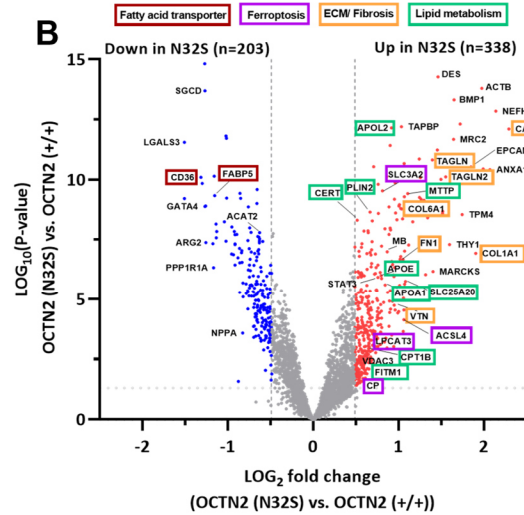
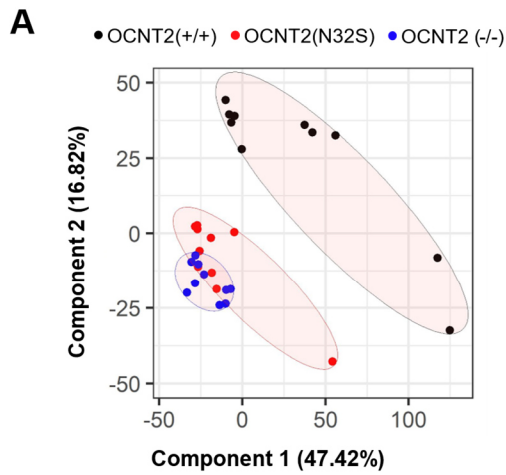


915
916
917
918
919
920
921
922

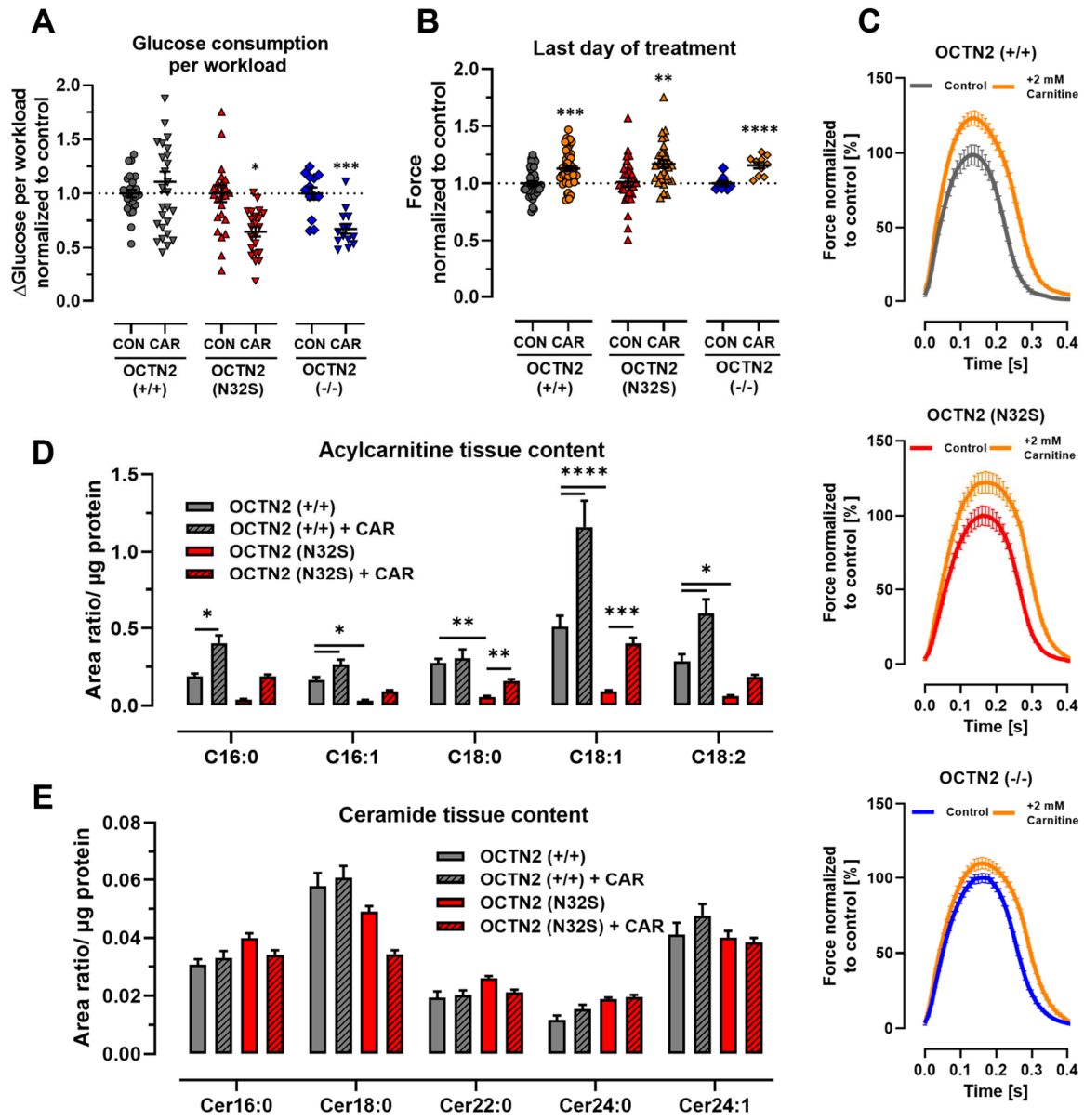
Figure 2. EHT contraction analysis and action potential measurement. **A:** Representative average EHT contraction peaks of OCTN2 (+/+), OCTN2 (N32S), OCTN2 (-/-). EHTs were electrically paced at 1.5 Hz in standard EHT medium, n=9-14 EHTs from one batch. **B:** Representative video-optical EHT images, scale bar: 1 mm. **C:** Representative action potential for OCTN2 (+/+) and OCTN2 (N32S). **D:** Action potential duration (APD₉₀) of OCTN2 (+/+) and OCTN2 (N32S) by sharp microelectrode measurement at 1.5 Hz. Student's t-test vs OCTN2 (+/+), *p<0.05. Data are expressed as mean±SEM. Each data point represents one EHT.



923
 924 **Figure 3. Pearson correlation of A: Force- and B: Resting length of EHTs with percentage of**
 925 **cTNT-positive input cells for EHT generation.** OCTN2 (+/+): n= 10; OCTN2 (N32S): n= 7 and
 926 OCTN2 (-/-): n= 7 differentiation batches. Each replicate represents the mean value of 7 to 20
 927 EHTs for the specific differentiation batch. **C:** EHT force development in fatty acid medium.
 928 Serum-free cell culture medium was supplemented with 50 μ M carnitine, linoleic acid- and
 929 oleic acid-albumin. Data are normalized to baseline force. OCTN2 (+/+): n=11 EHTs from 2
 930 batches, OCTN2 (N32S): n=11 EHTs from 2 batches, OCTN2 (-/-): n=12 EHTs from 2 batches.
 931 2-way ANOVA vs OCTN2 (+/+) followed by Bonferroni's post-test for multiple comparisons,
 932 * $p < 0.05$. Data are expressed as mean \pm SEM. **D:** Difference in Δ glucose media concentration
 933 divided by product of individual spontaneous beating frequency \times force. (Δ Glucose = Glucose
 934 concentration at baseline minus glucose concentration after 24 h of incubation) OCTN2 (+/+):
 935 n=59 EHTs from 5 batches, OCTN2 (N32S): n=51 EHTs from 4 batches, OCTN2 (-/-): n=28 EHTs
 936 from 4 batches. 1-way ANOVA followed by Bonferroni's post-test for multiple comparisons,
 937 * $p < 0.05$, ** $p < 0.01$, *** $p < 0.001$, **** $p < 0.0001$. One data point represents one EHT. Data are
 938 expressed as mean \pm SEM.

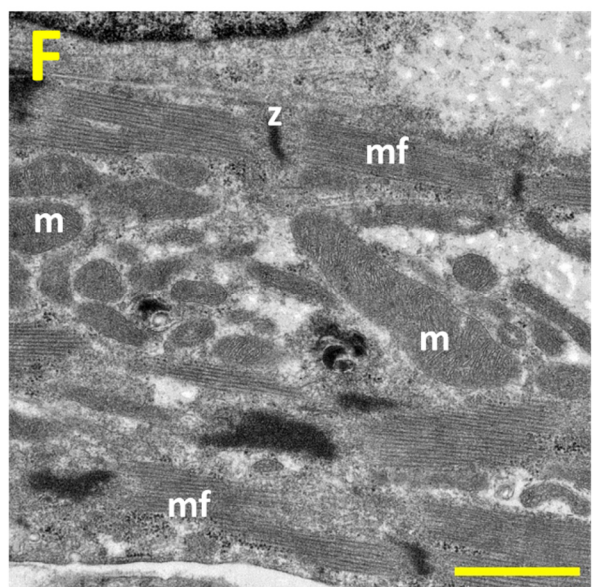
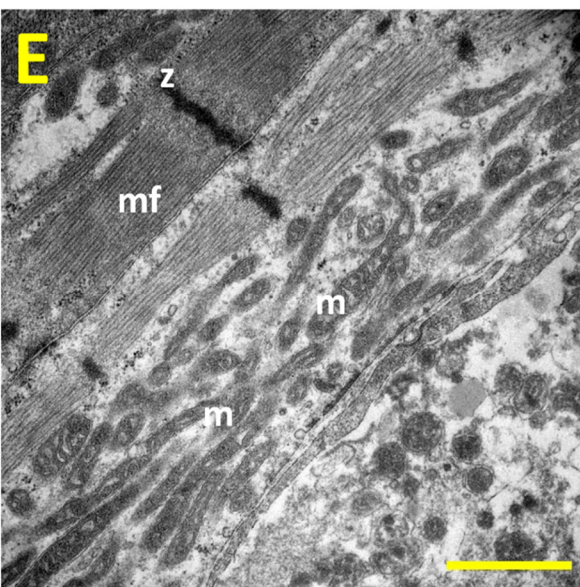
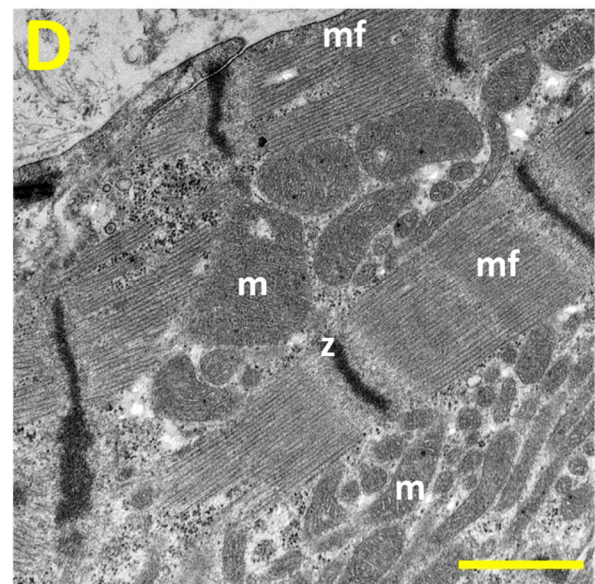
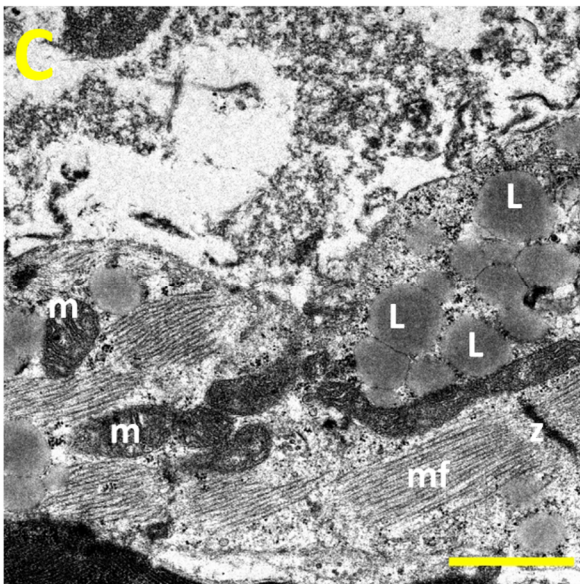
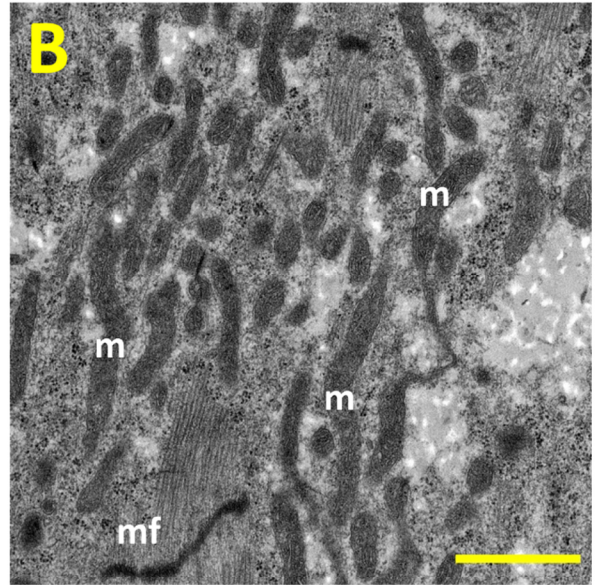
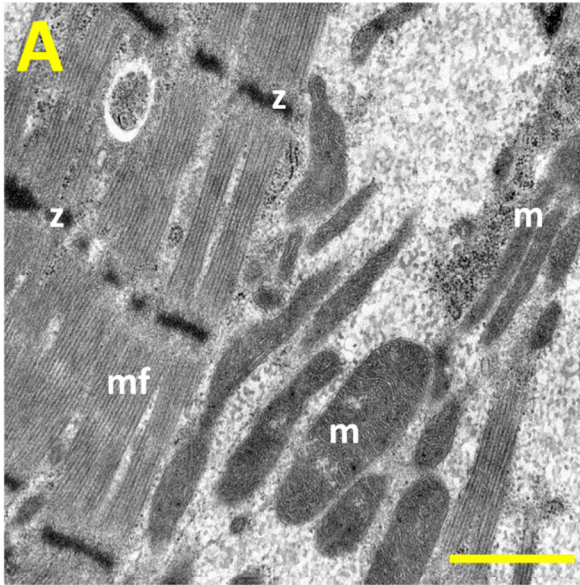


940 **Figure 4. TMT-based quantitative proteomic analysis of EHTs.** **A:** Principal component analysis
941 (PCA) of OCNT2 (+/+) (black, n=10) OCTN2 (N32S) (red, n=10) and OCTN2 (-/-) (blue, n=10)
942 EHTs based on their proteomic profiles. Each dot represents one EHT. **B:** Volcano plot of log₂
943 fold changes of OCTN2 (N32S) vs OCTN2 (+/+) and log₁₀ of the p values with color-coded
944 significance levels (p>0.05) and fold change >1.4. **C:** Clustering analysis of proteins related to
945 metabolic pathways. Heatmaps display the relative abundance of proteins involved in
946 glycolysis, carnitine shuttle, electron transport chain (ETC), beta-oxidation and TCA cycle, the
947 myocardium, lipid metabolism. OCNT2 (+/+): mean of 10 EHTs from 1 batch; OCTN2 (N32S):
948 mean of 10 EHTs from 1 batch; OCTN2 (-/-): mean of 10 EHTs from 1 batch. Protein levels are
949 depicted as a color code ranging from blue (low abundance) to red (high abundance). **D:**
950 Pathway enrichment analysis of proteins identified by proteomic analysis. Depicted are KEGG
951 pathways of significantly enriched proteins that were significantly higher (red) or lower (blue)
952 abundant in OCTN2 (N32S) vs OCTN2 (+/+), p<0.05, fold change >1.4.
953
954
955
956

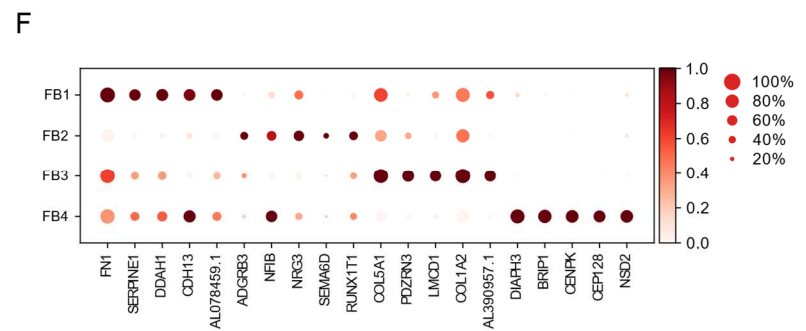
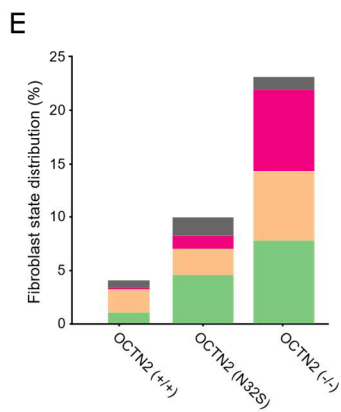
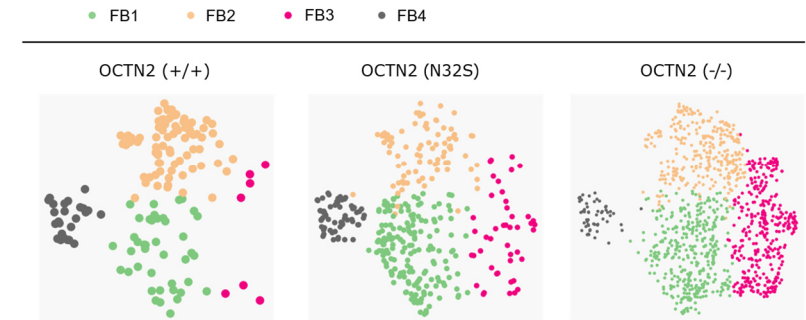
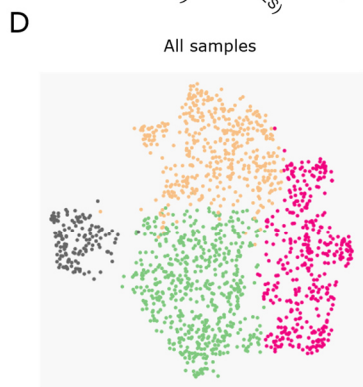
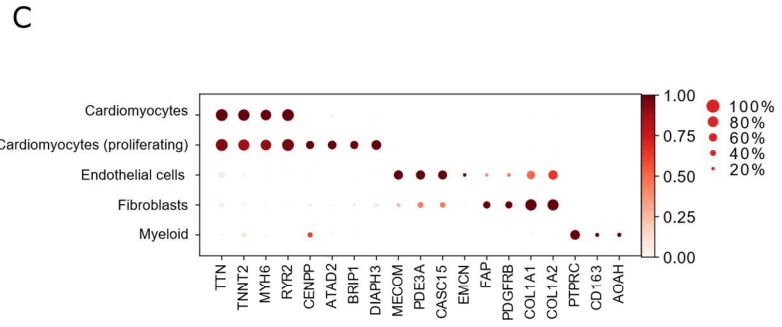
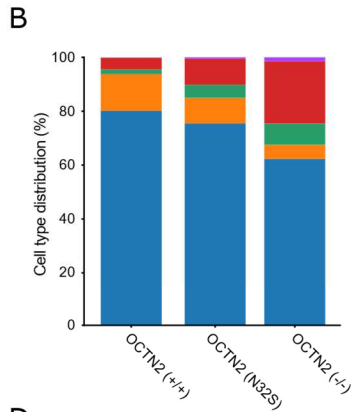
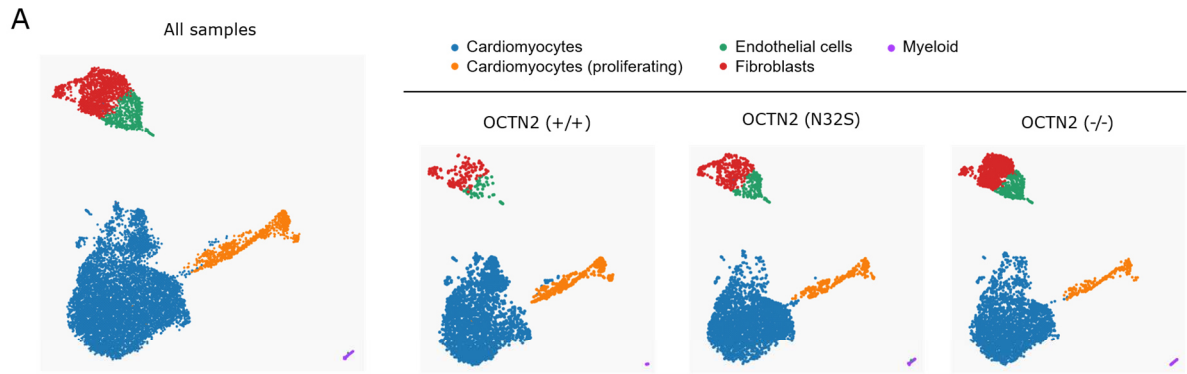


957
 958
 959
 960
 961
 962
 963
 964
 965
 966
 967
 968
 969
 970
 971
 972

973 **Figure 5. A: Effect of carnitine supplementation Δ glucose per workload** (Δ glucose= glucose
974 concentration at baseline minus glucose concentration after 24 hours of incubation; workload
975 = force \times frequency). Nested t-test vs CON, **p<0.01, ***p<0.001, ****p<0.0001. OCNT2 (+/+)
976 control: n=27 EHTs from 3 batches. OCNT2 (+/+) + carnitine (2 mM): n=28 EHTs from 3 batches.
977 OCTN2 (N32S) control: n=23 EHTs from 3 batches. OCTN2 (N32S) + carnitine (2 mM): n=23
978 EHTs from 3 batches, OCTN2 (-/-) control: n=13 EHTs from 3 batches, OCTN2 (-/-) + carnitine
979 (2 mM): n=16 EHTs from 3 batches. Data are expressed as mean \pm SEM. **B:** Effect of carnitine
980 supplementation on force of spontaneous beating EHTs at the last day of treatment (Day 33-
981 42). Values were normalized to last day of treatment of untreated control. Student's t-test vs
982 CON, **p<0.01, ***p<0.001, ****p<0.001. OCNT2 (+/+) control: n=54 EHTs from 4 batches.
983 OCNT2 (+/+) + carnitine (2 mM): n=49 EHTs from 4 batches. OCTN2 (N32S) control: n=36 EHTs
984 from 3 batches, OCTN2 (N32S) + carnitine (2 mM): n=33 EHTs from 3 batches, OCTN2 (-/-)
985 control: n=9 EHTs from 1 batch, OCTN2 (-/-) + carnitine (2 mM): n=9 EHTs from 1 batch. Data
986 are expressed as mean \pm SEM. **C:** Effect of carnitine supplementation on average contraction
987 peaks. Depicted are representative average EHT contraction peaks of OCTN2 (+/+),
988 OCTN2 (N32S), OCTN2 (-/-). EHTs were electrically paced at 1.5 Hz in standard EHT medium \pm
989 carnitine (2 mM). Values were normalized to untreated control. n= 9-16 EHTs per condition
990 from 1 batch. **D, E:** LC-MS- analysis of acylcarnitines and ceramides. Effect of carnitine
991 supplementation on **D:** Acylcarnitine- and **E:** ceramide content of OCNT2 (+/+) and
992 OCTN2 (N32S) EHTs after 33 days of culture and supplementation. 2-way ANOVA followed by
993 Bonferroni's post-test for multiple comparisons, *p<0.05, **p<0.01, ***p<0.001,
994 ****p<0.0001. Data are expressed as mean \pm SEM. n=4 EHT pools (containing 3 EHTs each) per
995 genotype and carnitine supplementation from 1 batch.

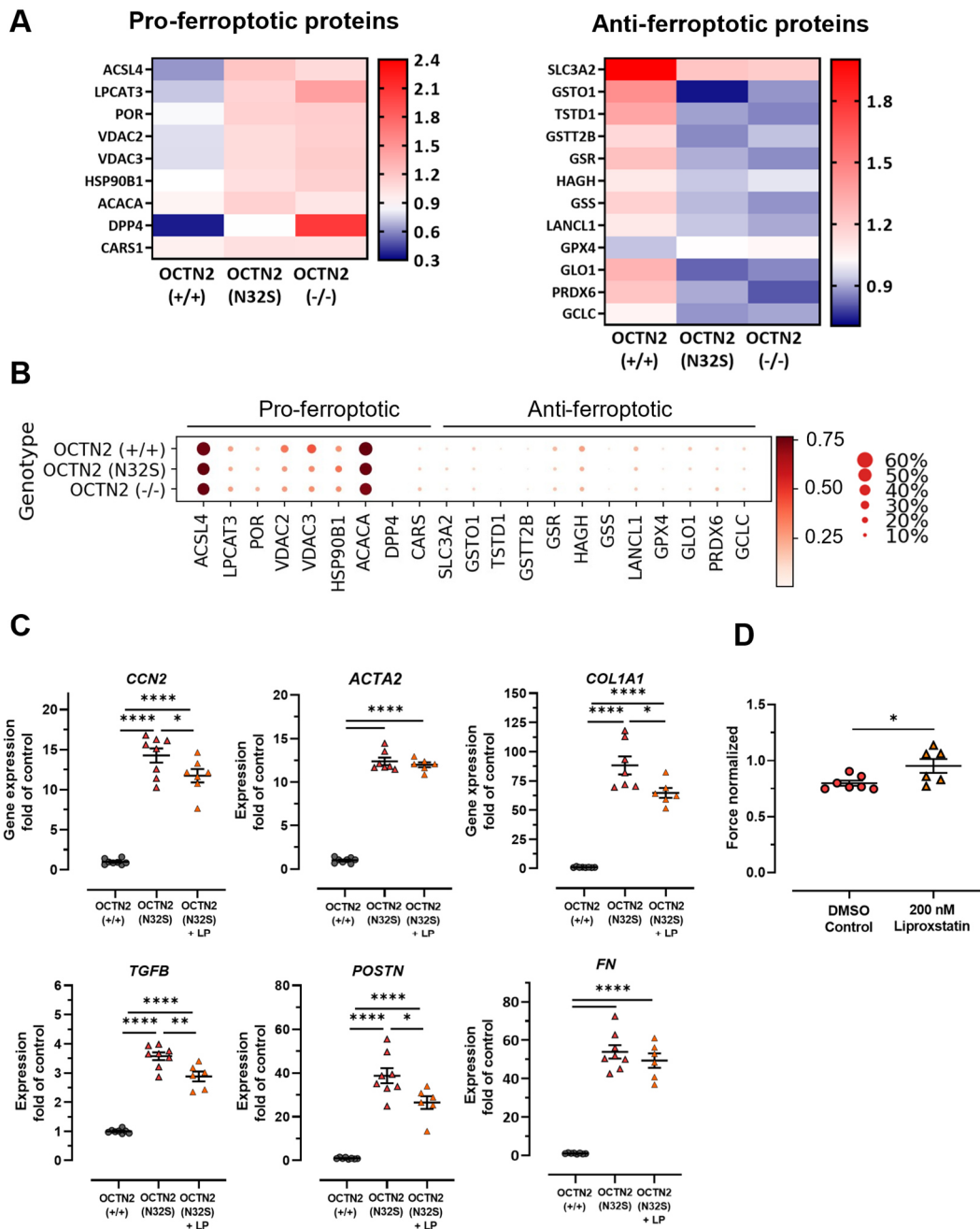


997 **Figure 6. Transmission electron microscopy of OCTN2 EHTs.** A + B: OCTN2 (+/+), C + D: OCTN2
998 (N32S), E + F: OCTN2 (-/-). A, C and E untreated, B, D and F supplemented with carnitine (2
999 mM). mf: myofilaments, z: z-line, m: mitochondria, L: lipid droplet. Scale bar = 1 μ m.
1000
1001

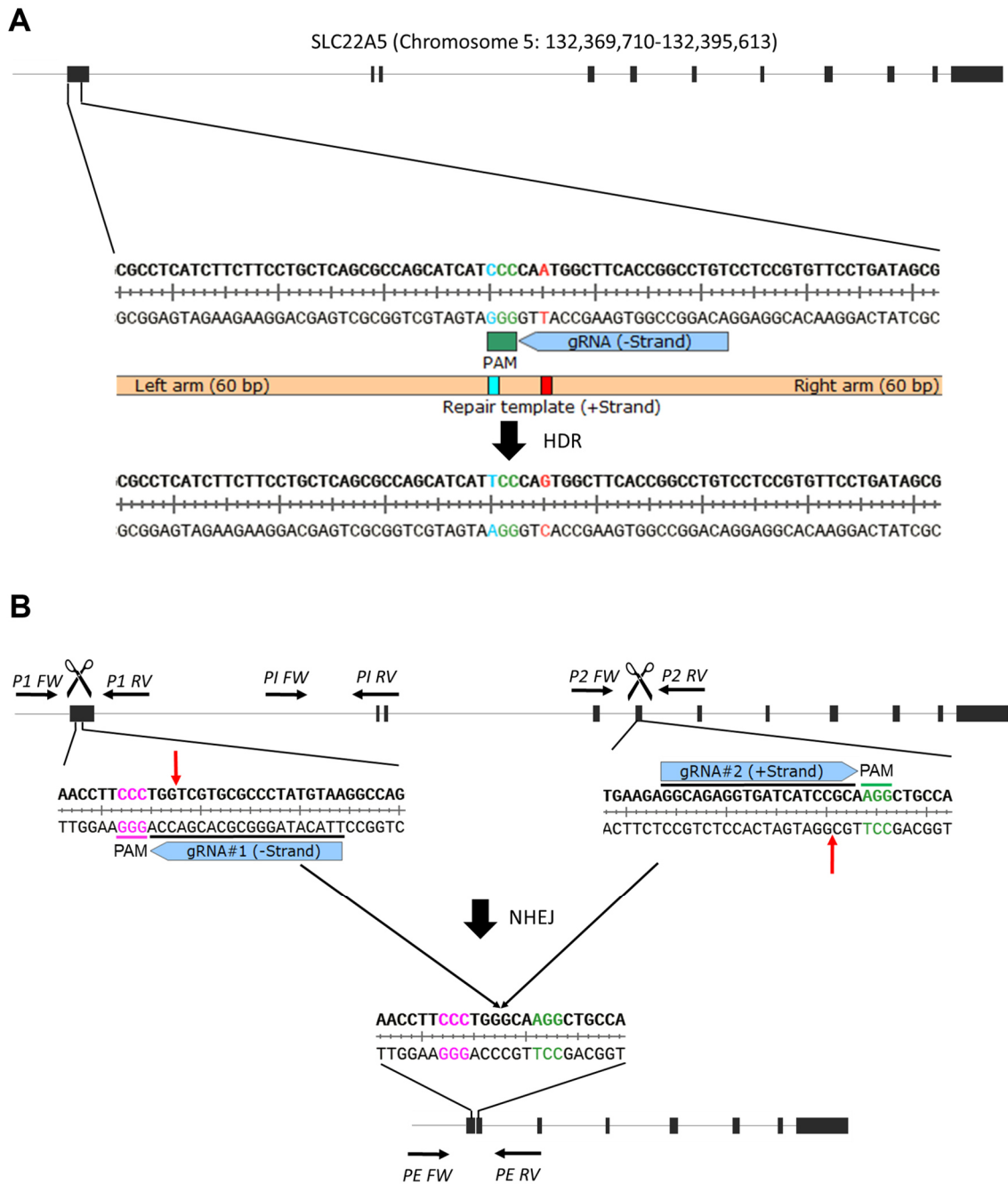


1002
 1003
 1004
 1005

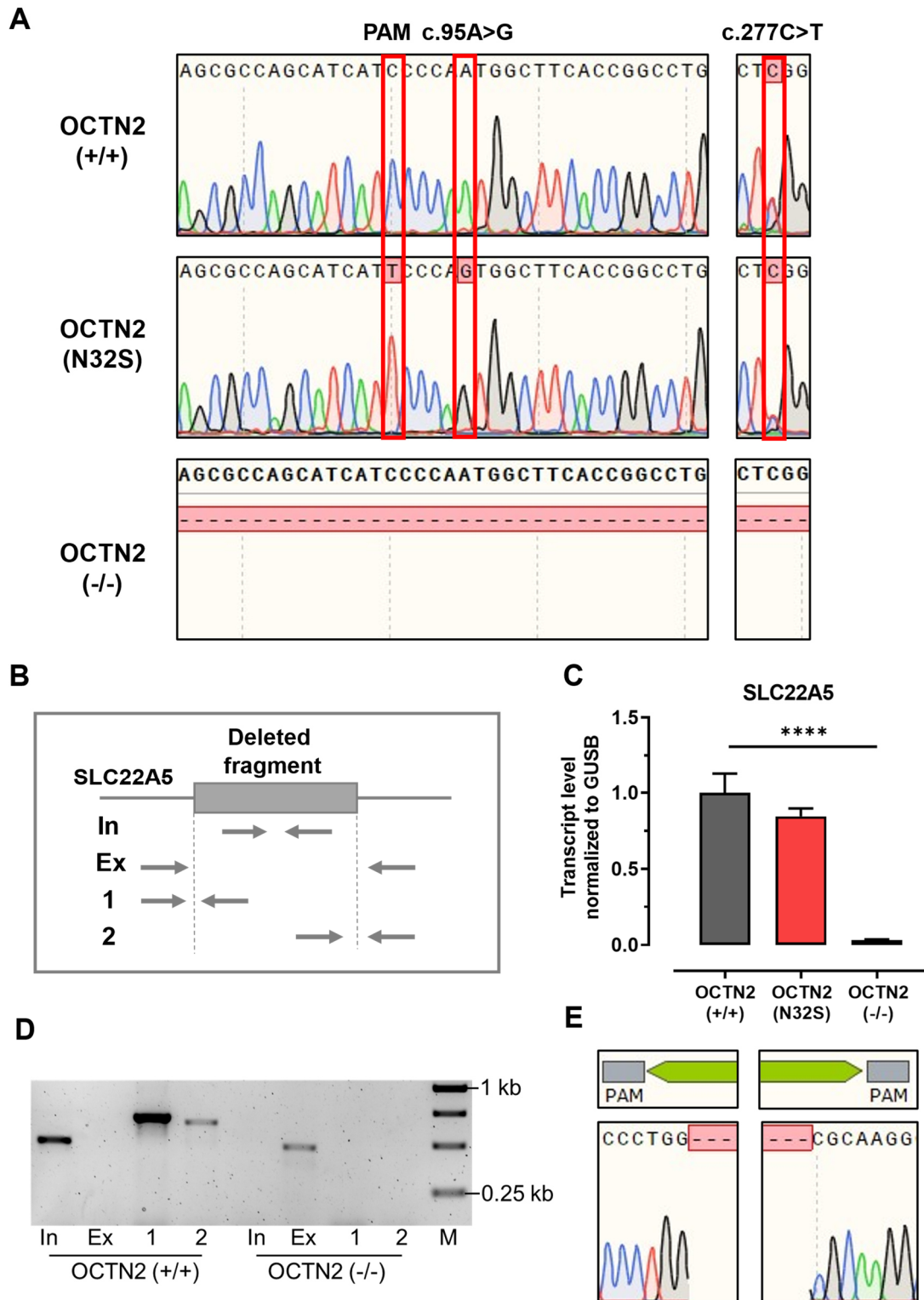
1006 **Figure 7. Cellular heterogeneity in OCTN2 genotypes in EHTs.** **A:** Representative UMAP plot
1007 after single-nucleus RNA sequencing of all samples and individual genotypes, n=1 EHT pool (4
1008 EHTs) per genotype; OCTN2 (+/+) (3674 cells), OCTN2 (N32S) (4525 cells) OCTN2 (-/-) (5108
1009 cells). 5 distinct cell clusters were identified: cardiomyocytes, cardiomyocytes (proliferating),
1010 endothelial cells, fibroblasts and myeloid cells. **B:** Percentage of cell types per genotype. **C:** Dot
1011 plot graph showing the relative expression of cell-specific marker genes. Expression levels are
1012 depicted as a color code ranging from light red (low expression) to dark red (high expression)
1013 as mean of log₂ fold of expression. **D:** Representative fibroblast subcluster FB1-4 UMAP plot
1014 of all samples and individual genotypes. **E:** Percentage of fibroblast states per genotype. For
1015 each genotype, the total percentage of fibroblast states equals the percentage of fibroblast
1016 abundance identified in B. **F:** Dot plot graph showing the relative expression of fibroblast-
1017 specific marker genes in fibroblast states. Scaled expression levels are depicted as a color code
1018 ranging from light red (low expression) to dark red (high expression) as mean of log₂ fold of
1019 expression.



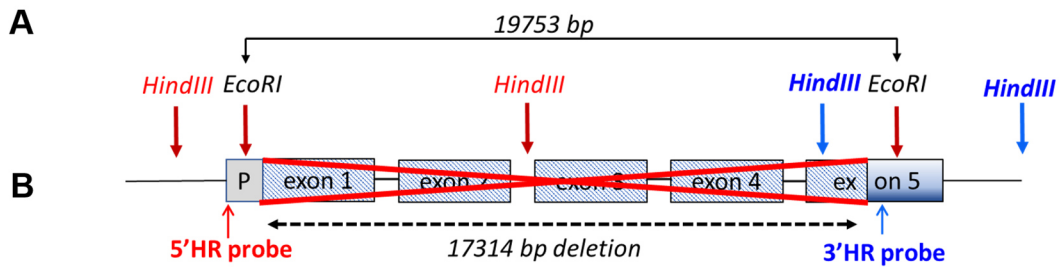
1020 **Figure 8. Evidence for ferroptosis pathway activation in TMT-based quantitative proteomic**
 1021 **analysis and pharmacological inhibitor experiments. A: Proteomic analysis heatmaps display**
 1022 **the relative abundance of pro- and anti-ferroptotic proteins of all genotypes. OCNT2 (+/+):**
 1023 **mean of 10 EHTs from 1 batch; OCTN2 (N32S): mean of 10 EHTs from 1 batch; OCTN2 (-/-):**
 1024 **mean of 10 EHTs from 1 batch. Protein levels are depicted as a color code ranging from blue**
 1025 **(low abundance) to red (high abundance). B: Single-nucleus RNA sequencing dot plot graph**
 1026 **showing the scaled relative expression of pro- and anti-ferroptotic markers across all**
 1027 **genotypes for all cells. C: Effect of ferroptosis inhibitor liproxstatin: Quantitative PCR analysis**
 1028 **of gene expression genes related to fibroblast activation. Gene expression was normalized to**
 1029 **GUSB over OCTN2 (+/+) control. OCNT2 (+/+): n=8 EHTs from 2 batches, OCTN2 (N32S): n=8**
 1030 **EHTs from 2 batches; OCTN2 (-/-): n=6-8 EHTs from 1 batches. 1-way ANOVA followed by**
 1031 **Bonferroni's post-test for multiple comparisons, *p<0.05, **p<0.01, ****p<0.0001. Data are**
 1032 **expressed as mean±SEM. D: Effect of liproxstatin (200nM) on contractile force in OCTN2**
 1033 **(N32S) EHTs. Data are expressed as mean±SEM, *p<0.05, unpaired t-test.**



1036 **Supplementary Figure 1. A:** Schematic overview of CRISPR/Cas9 strategy for OCTN2 (N32S)
 1037 generation. A ssODN containing the desired point mutation was co-transfected with CRISPR
 1038 components to introduce the mutation c.95A>G, p.N32S in exon1 of the *SLC22A5* gene.
 1039 Depicted is the gRNA target site and the predictive DNA sequence after successful integration
 1040 of the repair template. **B:** Schematic overview over CRISPR/Cas9 strategy for OCTN2 (-/-)
 1041 generation. Two gRNA were co-transfected to induce simultaneous cutting and a large deletion
 1042 in the *SLC22A5* gene. Depicted are the gRNA target sites and the predictive DNA sequence
 1043 after successful editing. Red arrows indicate the predicted Cas9 cutting sites. Black arrows
 1044 indicate the primer binding sites for PCR validation. P1: Primer target region gRNA1; P2: Primer
 1045 target region gRNA2; PI: Primer internal; PE: Primer external; Pink: PAM1; Green: PAM2.

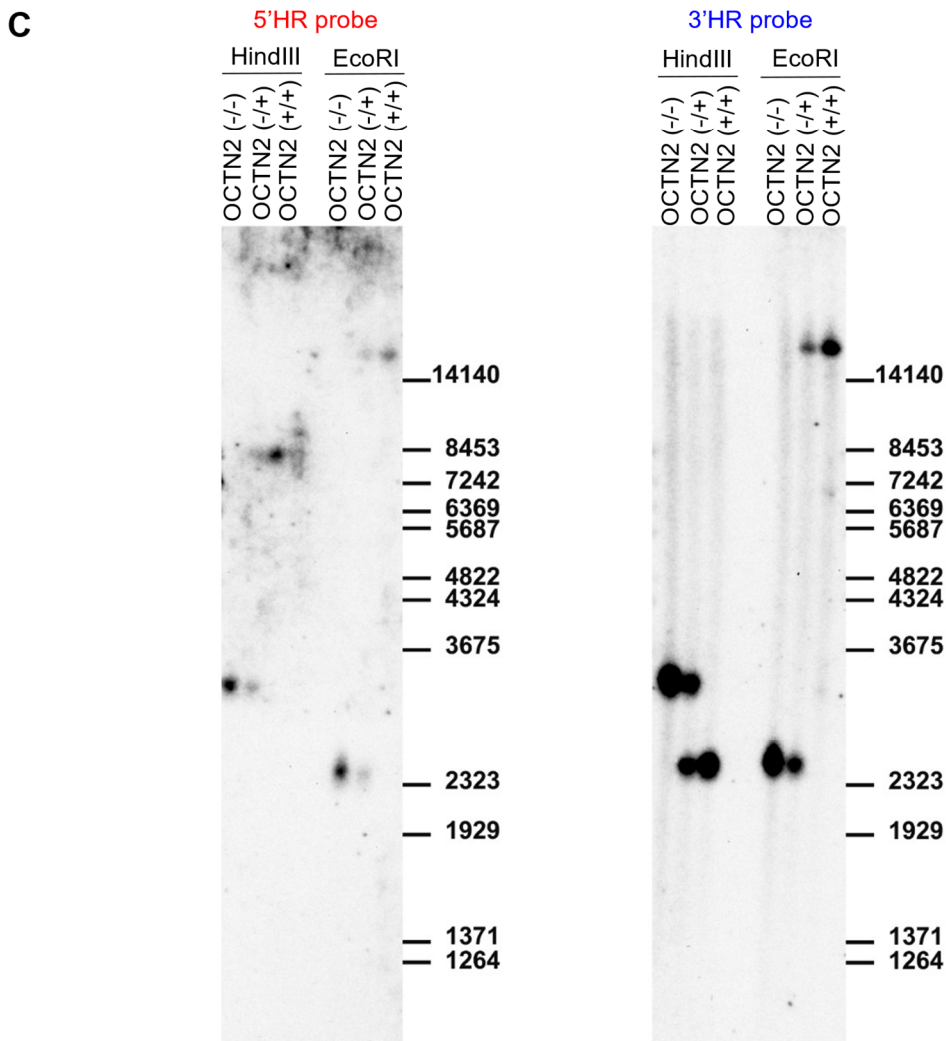


1046 **Supplementary Figure 2. Genotype characterization of CRISPR/Cas9-edited hiPSCs.** **A:** Sanger
 1047 sequencing traces of OCTN2 (+/+) and derived single cell clones for OCTN2 (N32S) and
 1048 OCTN2 (-/-) genotypes. The red boxes indicate the silent PAM- and c.95A>G mutation and the
 1049 heterozygous silent c277C>T mutation in the OCTN2 (N32S) clone. **B:** Schematic overview of
 1050 primer localization in relation to the deleted fragment in the *SLC22A5* gene. **C:** qPCR analysis
 1051 of *SLC22A5* transcripts for all genotypes. **D:** Gel electrophoresis of PCR products of OCTN2 (+/+) and
 1052 OCTN2 (-/-) hiPSC clones; M = 1 kb DNA standard marker. **E:** Sanger sequencing trace of
 1053 OCTN2 (-/-) PCR product amplified with external primers. Depicted are the binding sites of
 1054 both gRNA.

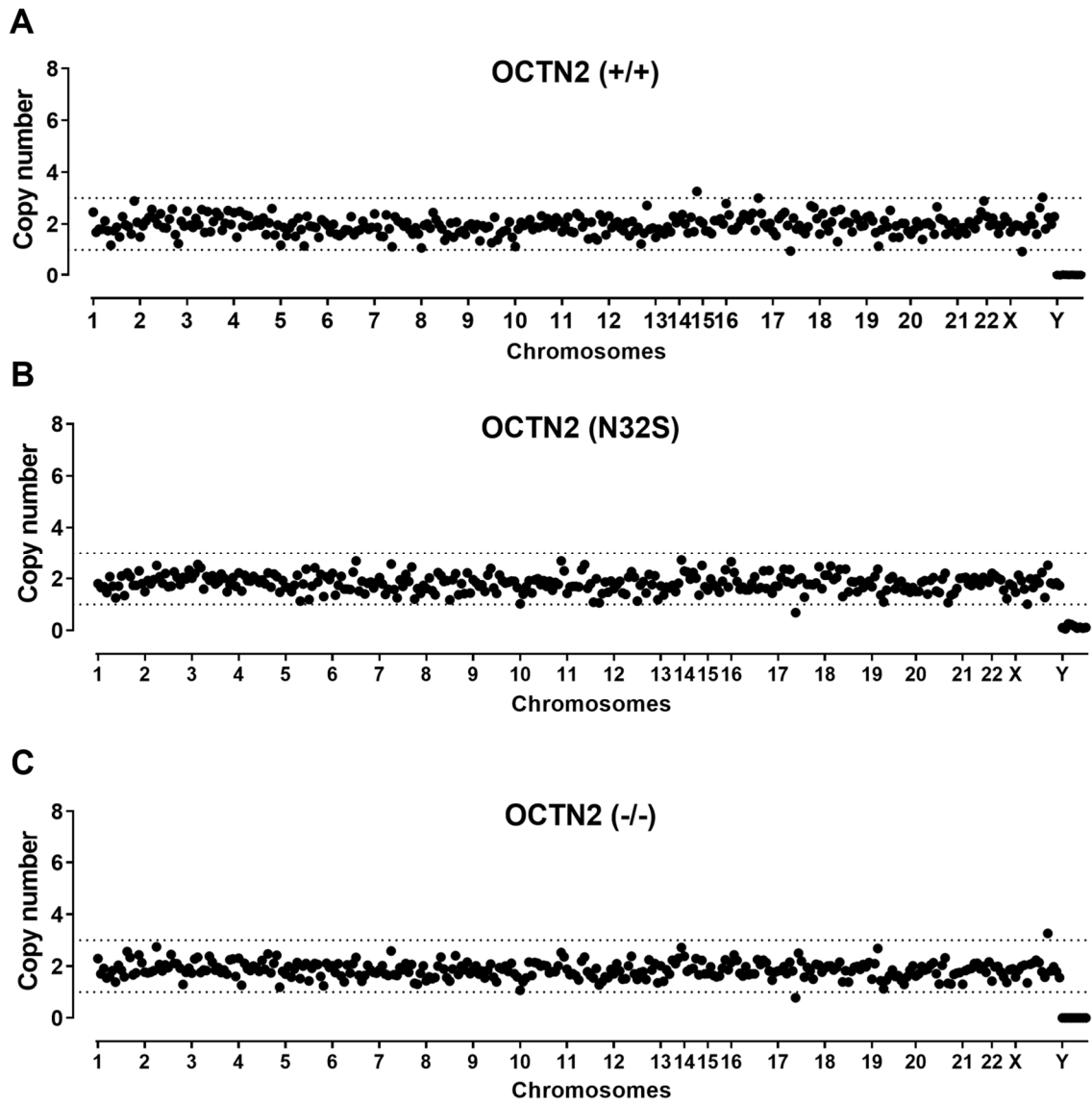


5'HR probe
 HindIII: (wt: 8292 bp; deleted: 3264 bp)
 EcoRI: (wt: 19753 bp; deleted: 2439 bp)

3'HR probe
 HindIII: (wt: 2434 bp; deleted: 3264 bp)
 EcoRI: (wt: 19753 bp; deleted: 2439 bp)



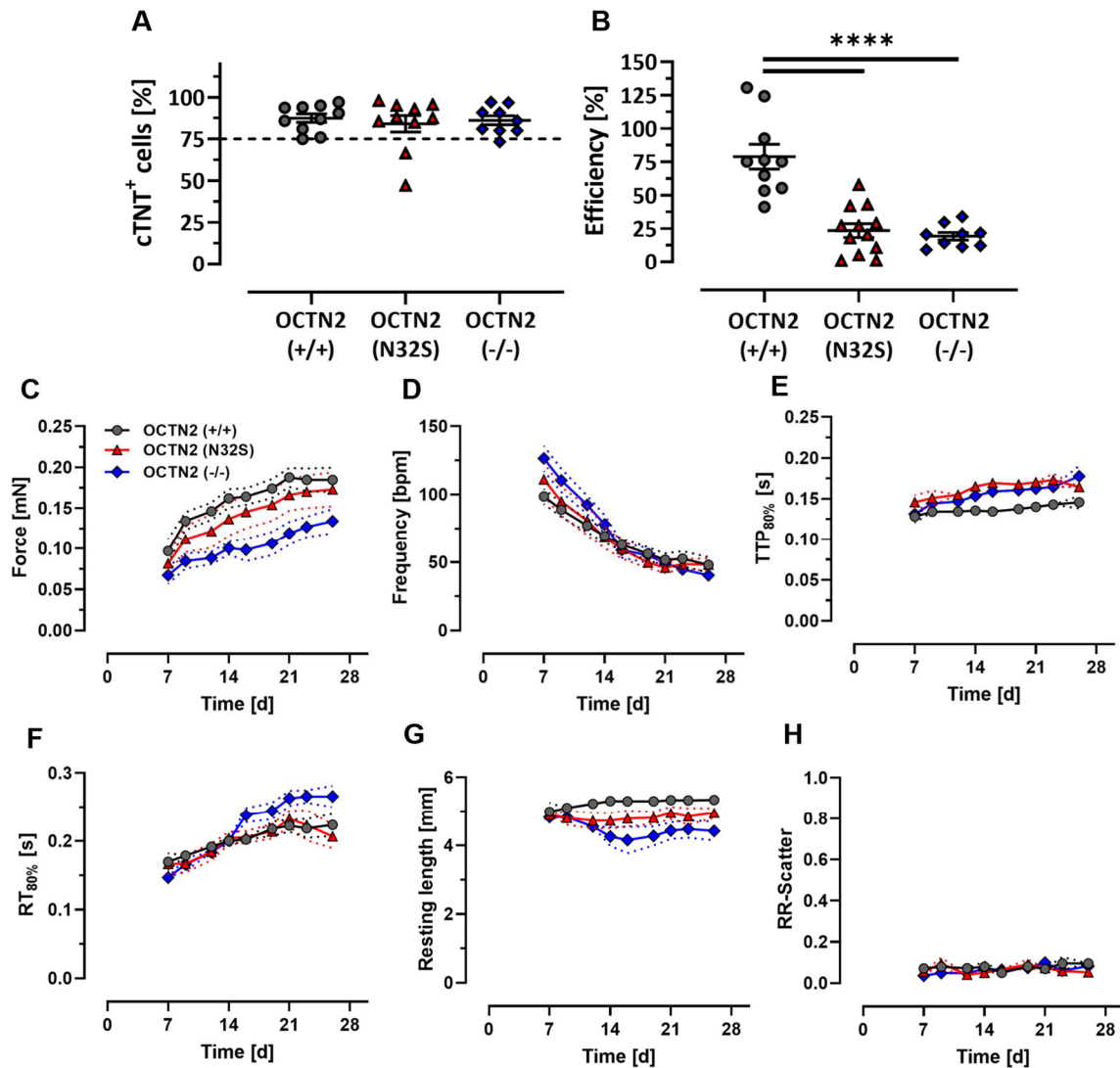
1057 **Supplementary Figure 3. Southern blot analysis of genomic DNA from OCTN2 (+/+), OCTN2**
 1058 **(-/+)** and **OCTN2 (-/-)** hiPSC. **A:** Schematic presentation of Southern blot probes hybridization
 1059 position. HindIII and EcoRI enzymes were used for enzymatic digestion of genomic DNA
 1060 samples. **B:** Fragment size prediction of 5' HR and 3'HR hybridization after HindIII or EcoRI
 1061 restriction enzyme digest. **C:** Southern blot analysis of OCTN2 (+/+), OCTN2 (-/+), and OCTN2 (-/
 1062 -/) hiPSC.



1063

1064 **Supplementary Figure 4. Nanostring karyotype analysis of hiPSC master cell bank samples.**

1065 **A: OCTN2 (+/+), B: OCTN2 (N32S) and C: OCTN2 (-/-).**



1066

1067

1068

1069

1070

1071

1072

1073

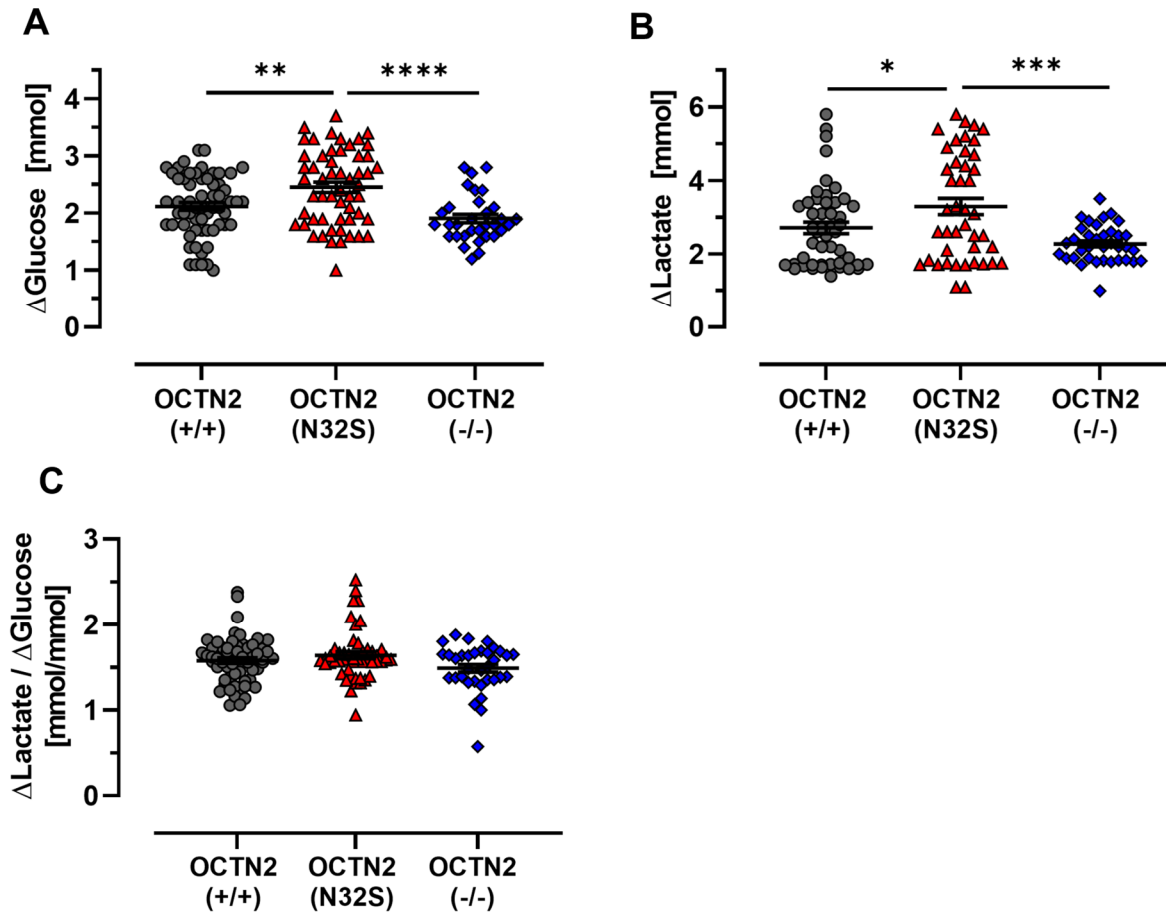
1074

1075

1076

1077

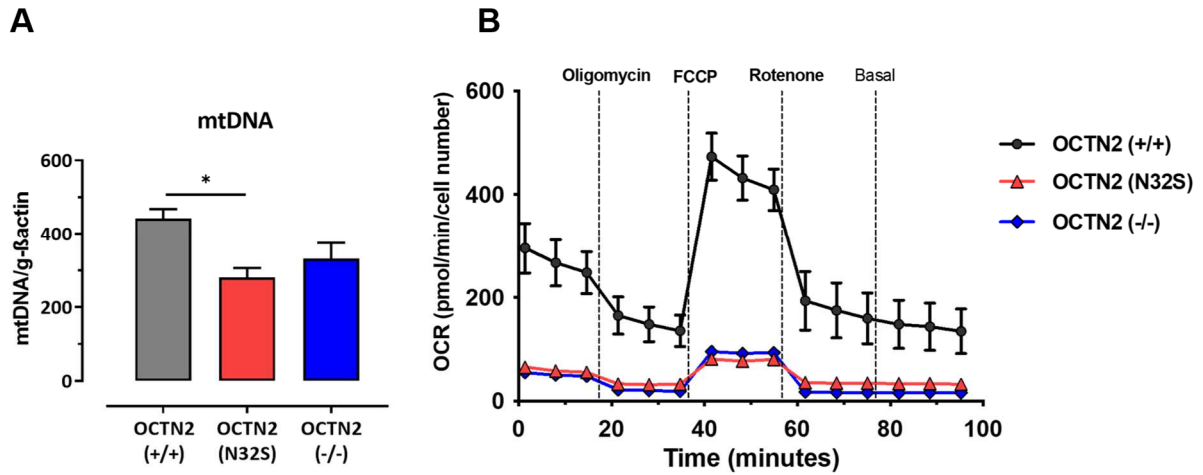
Supplementary Figure 5. Characterization of cardiomyocyte differentiations and contractile parameters. **A**: FACS analysis of cardiac troponin T-positive cells in the differentiated cell population. The dashed line (75%) indicates threshold value for EHT generation. **B**: Differentiation efficiency calculated as the ratio of number of differentiated cells divided by the number of input hiPSCs. OCTN2 (+/+): n=10, OCTN2 (N32S): n=10, OCTN2 (-/-): n=9 differentiation batches, data are expressed as mean±SEM, 1-way ANOVA followed by Bonferroni's post-test for multiple comparisons, ****p<0.0001. **C-H**: Effect of OCTN2 genotype on force, frequency, contraction time (TTP_{80%}), relaxation time (RT_{80%}), resting length and RR-Scatter (parameter of irregularity) of spontaneous beating EHTs between day 7 and day 26. OCTN2 (+/+): n=152 EHTs from 9 batches, OCTN2 (N32S): n=108 EHTs from 7 batches, OCTN2 (-/-): n=91 EHTs from 5 batches, data are expressed as EHT batch mean±SEM.



1078

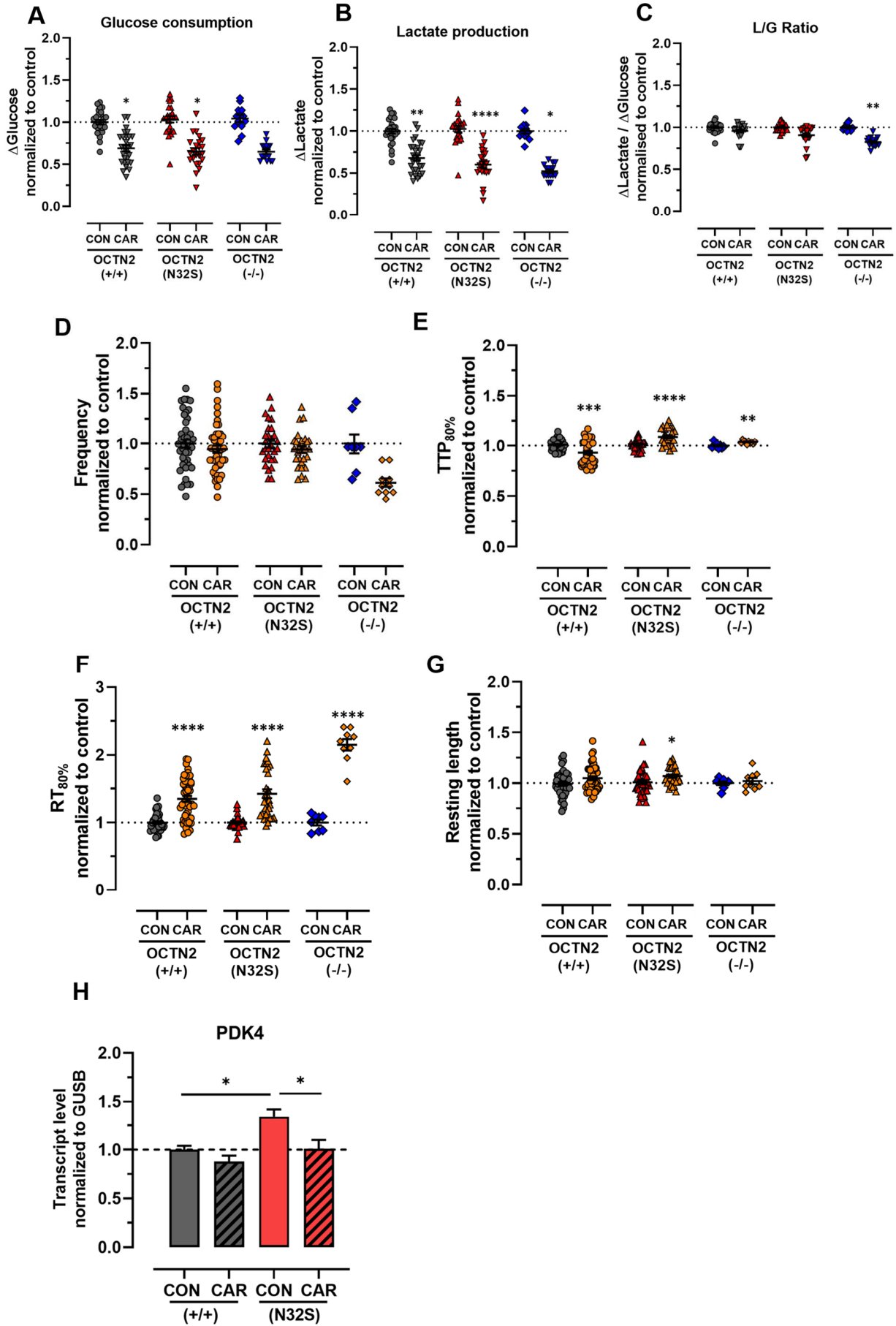
1079 **Supplementary Figure 6. Glucose- and lactate measurements.** Difference in **A**: Glucose- and
 1080 **B**: Lactate concentration of EHT culture media (Δ glucose = glucose concentration at baseline
 1081 minus glucose concentration after 24 h of incubation, Δ lactate = lactate concentration at
 1082 baseline minus lactate concentration after 24 h of incubation). **C**: Δ Lactate of EHT culture
 1083 media divided by Δ glucose. OCTN2 (+/+): n=59 EHTs from 5 batches, OCTN2 (N32S): n=51 EHTs
 1084 from 4 batches, OCTN2 (-/-): n=28 EHTs from 4 batches. 1-way ANOVA followed by Bonferroni's
 1085 post-test for multiple comparisons, *p<0.05, **p<0.01, ***p<0.001, ****p<0.0001. One data
 1086 point represents one independent EHT. Data are expressed as mean \pm SEM.

1087

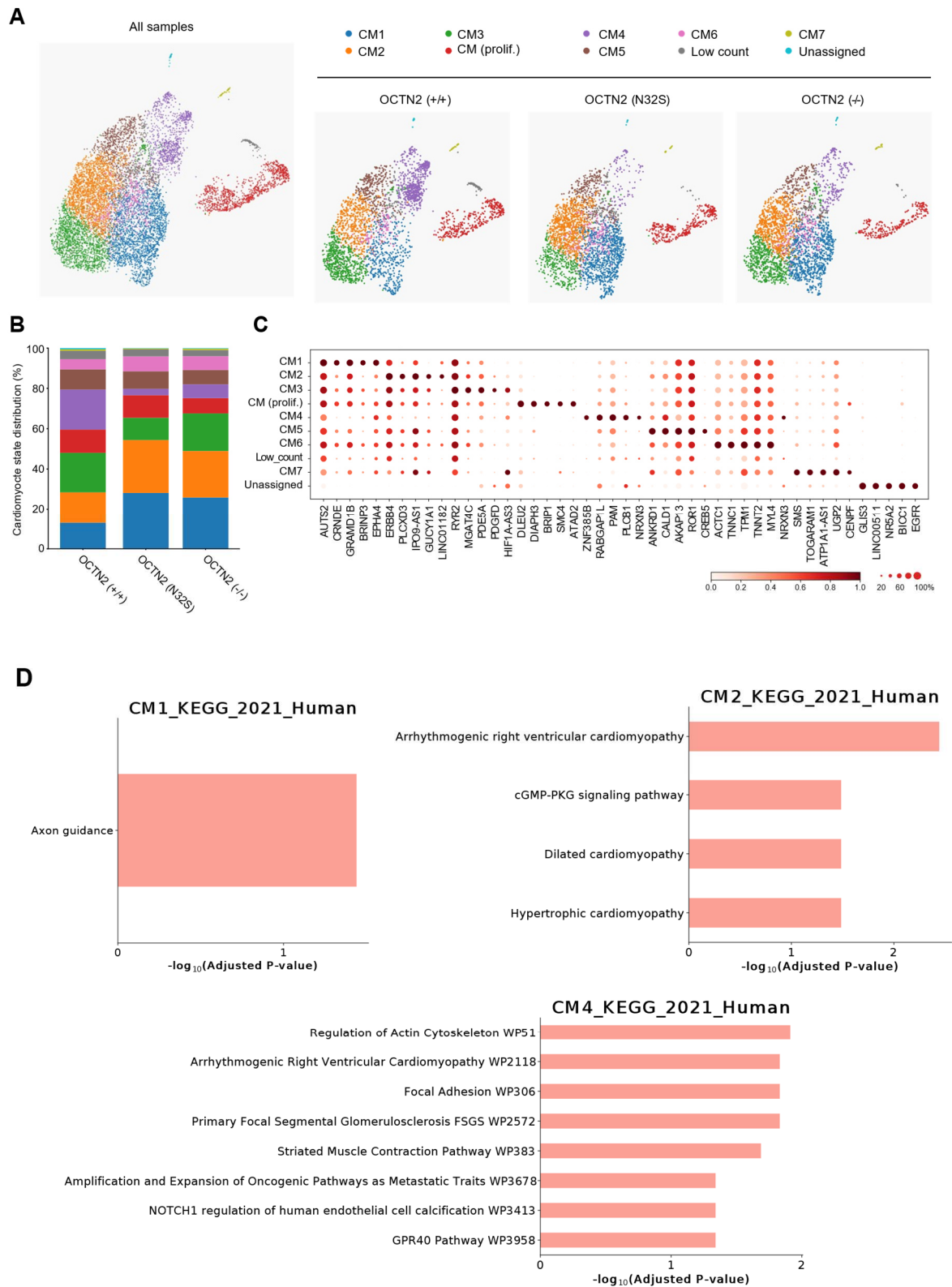


1088

1089 **Supplementary Figure 7. A: Effect of OCTN2 genotype on mitochondrial DNA analyzed by**
 1090 **quantitative PCR.** MtDNA was normalized to nuclear-encoded globular actin (g-actin). OCTN2
 1091 (+/+): n=5 EHTs from 1 batch, OCTN2 (N32S): n=7 EHTs from 1 batch, OCTN2 (-/-): n=7 EHTs
 1092 from 1 batch. 1-way ANOVA followed by Bonferroni's post-test for multiple comparisons,
 1093 *p<0.05. Data are expressed as mean±SEM. **B:** Oxygen consumption rate in OCTN2 (+/+),
 1094 (N32S) and (-/-). Mean ± SEM, n=2 biological replicates (each biological replicate represents
 1095 the average of 12 wells of a 96-well Seahorse plate), Mann-Whitney U test, *p<0.05.

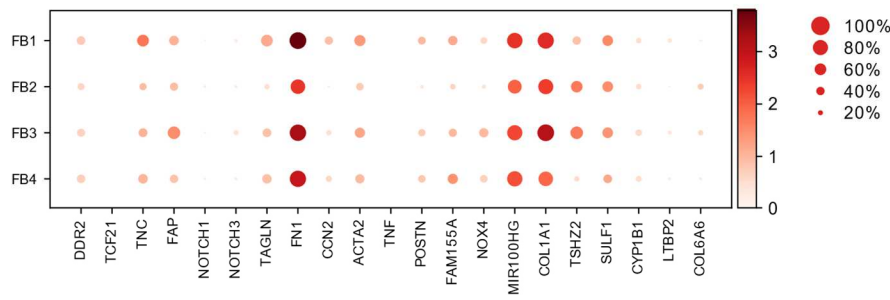


1097 **Supplementary Figure 8. A-C: Effect of carnitine supplementation on glucose consumption**
1098 **and lactate production. A:** Δ Glucose (Δ glucose= glucose concentration at baseline minus
1099 glucose concentration after 24 hours of incubation); **B:** Δ Lactate (Δ lactate= lactate
1100 concentration after 24 hours of incubation minus lactate concentration at baseline). Nested t-
1101 test vs CON, **p<0.01, ***p<0.001, ****p<0.0001. OCNT2 (+/+) control: n=27 EHTs from 3
1102 batches. OCNT2 (+/+) + carnitine (2 mM): n=28 EHTs from 3 batches. OCTN2 (N32S) control:
1103 n=23 EHTs from 3 batches. OCTN2 (N32S) + carnitine (2 mM): n=23 EHTs from 3 batches,
1104 OCTN2 (-/-) control: n=13 EHTs from 3 batches, OCTN2 (-/-) + carnitine (2 mM): n=16 EHTs from
1105 3 batches. Data are expressed as mean \pm SEM. **D-G:** Effect of carnitine supplementation on
1106 spontaneous beating EHTs at the last day of treatment (Day 33-42). **D:** Frequency, **E:** Time to
1107 peak, **F:** Relaxation time and **G:** Resting length. Values were normalized to last day of treatment
1108 of untreated control. Student's t-test vs CON, **p<0.01, ***p<0.001, ****p<0.001. OCNT2
1109 (+/+) control: n=54 EHTs from 4 batches. OCNT2 (+/+) + carnitine (2 mM): n=49 EHTs from 4
1110 batches. OCTN2 (N32S) control: n=36 EHTs from 3 batches, OCTN2 (N32S) + carnitine (2 mM):
1111 n=33 EHTs from 3 batches, OCTN2 (-/-) control: n=9 EHTs from 1 batch, OCTN2 (-/-) + carnitine
1112 (2 mM): n=9 EHTs from 1 batch. Data are expressed as mean \pm SEM. **H:** Effect of carnitine
1113 supplementation on PDK4 mRNA expression. OCNT2 (+/+) and OCTN2 (N32S) EHTs were
1114 treated over the entire culture time harvested on day 42. Gene expression was normalized to
1115 GUSB over OCTN2 (+/+) control. n=7 EHTs per genotype and carnitine treatment from 1 batch.
1116 2-way ANOVA followed by Bonferroni's post-test for multiple comparisons, *p<0.05. Data are
1117 expressed as mean \pm SEM.

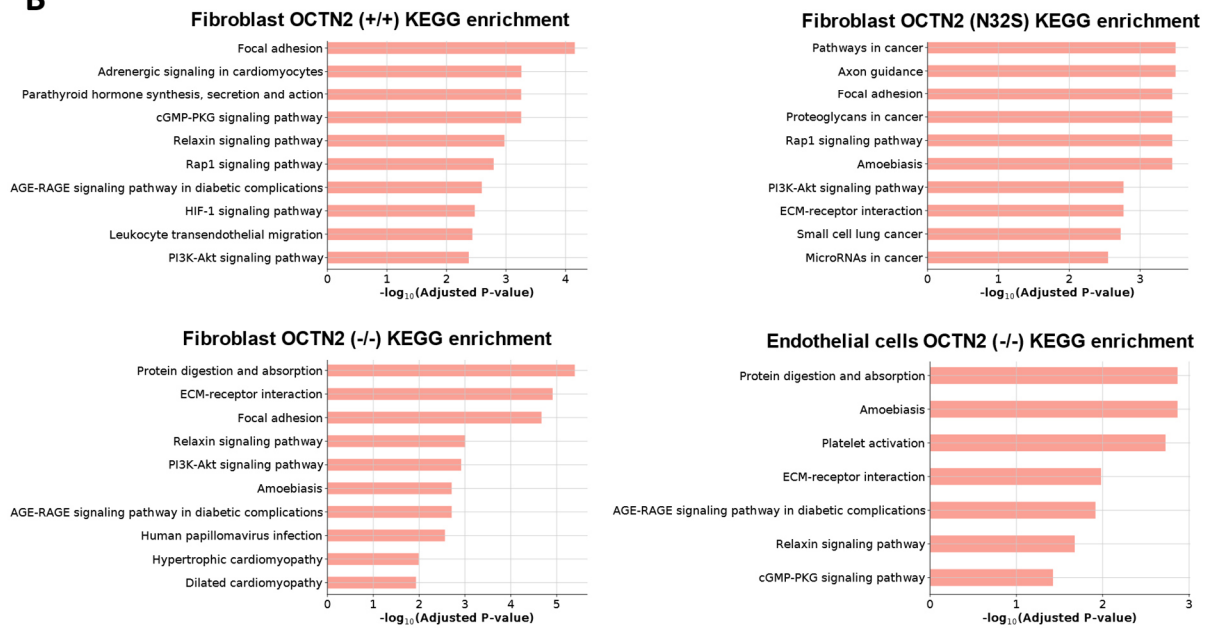


1118 **Supplementary Figure 9. Cardiomyocyte and fibroblast subcluster analysis in OCTN2**
 1119 **genotypes. A:** Representative UMAP plot after single-nucleus RNA sequencing of all samples
 1120 and individual genotypes. **B:** Percentage of cardiomyocyte subcluster per genotype. **C:** Dot plot
 1121 graph showing the relative expression of upregulated genes per cell cluster. Expression levels
 1122 are depicted as a color code ranging from light red (low expression) to dark red (high
 1123 expression) as mean of log₂ fold of expression. **D:** Enrichment analysis of significantly
 1124 upregulated genes from cardiomyocyte subclusters CM1, CM2, CM4.

A



B



1125

1126

1127

1128

1129

1130

1131

1132

Supplementary Figure 10. Fibroblast and endothelial cell subcluster analysis in OCTN2 genotypes. A: Dot plot graph showing the relative expression of specific marker genes related fibroblast activation in fibroblast states. Unscaled expression levels are depicted as a color code ranging from light red (low expression) to dark red (high expression) as mean of log₂ fold of expression. **B:** Enrichment analysis of significantly upregulated genes from fibroblast and endothelial cell subclusters. OCTN2 (+/+) and OCTN2 (N32S) endothelial cell and all myeloid subclusters did not reveal significant enriched pathways.

- 1133 Supplementary Tables
- 1134 Supplementary Table 1. Detected proteins proteomic analysis
- 1135 Supplementary Table 2. KEGG Enrichment analysis of proteins with significant higher
1136 abundance in OCTN2 (N32) vs OCTN2 (++)
- 1137 Supplementary Table 3. KEGG Enrichment analysis of proteins with significant lower
1138 abundance in OCTN2 (N32) vs OCTN2 (++)
- 1139 Supplementary Table 4. Composition of stem cell related culture media
- 1140 Supplementary Table 5. SsODN- and gRNA sequences
- 1141 Supplementary Table 6. Primer pairs for PCR and Sanger sequencing
- 1142 Supplementary Table 7. Primary antibodies used for flow cytometry/FACS
- 1143 Supplementary Table 8. Primer pairs for qPCR
- 1144 Supplementary Table 9. Primer pairs for 5'HR probe and 3' HR probe design
1145
- 1146 Supplementary Videos
- 1147 Supplementary Video 1. Spontaneously beating OCTN2 (+/+) EHT
- 1148 Supplementary Video 2. Spontaneously beating OCTN2 (N32S) EHT
- 1149 Supplementary Video 3. Spontaneously beating OCTN2 (-/-) EHT

Supplementary Files

This is a list of supplementary files associated with this preprint. Click to download.

- [SupplementaryTable1.Detectedproteinsproteomicanalysis.xlsx](#)
- [SupplementaryTable2KEGGENrichmentanalysisofproteinswithsignificanthigherabundanceinOCTN2N32vsOCTN2.xlsx](#)
- [SupplementaryTable3KEGGENrichmentanalysisofproteinswithsignificantlowerabundanceinOCTN2N32vsOCTN2.xlsx](#)
- [SupplementaryTables49.pdf](#)
- [SupplementaryVideo1.SpontaneouslybeatingOCTN2EHT.avi](#)
- [SupplementaryVideo2.SpontaneouslybeatingOCTN2N32SEHT.avi](#)
- [SupplementaryVideo3SpontaneouslybeatingOCTN2EHT.avi](#)